

# Hydrodynamic theory of wetting by active particles

Noah Grodzinski<sup>1,\*</sup>, Robert L. Jack<sup>1,2</sup>, and Michael E. Cates<sup>1</sup>

<sup>1</sup>*Department of Applied Mathematics and Theoretical Physics,*

*University of Cambridge, Wilberforce Road, Cambridge, United Kingdom and*

<sup>2</sup> *Yusuf Hamied Department of Chemistry, University of Cambridge, Lensfield Road, Cambridge, United Kingdom*

(Dated: June 18, 2025)

The accumulation of self-propelled particles on repulsive barriers is a widely observed feature in active matter. Despite being implicated in a broad range of biological processes, from biofilm formation to cytoskeletal movement, wetting of surfaces by active particles remains poorly understood. In this work, we study this active wetting by considering a model comprising an active lattice gas, interacting with a permeable barrier under periodic boundary conditions, for which an exact hydrodynamic description is possible. Our model eliminates dynamical noise while retaining microscopic fidelity, enabling a precise characterisation of steady-states and their transitions. We demonstrate that the accumulation of active particles is remarkably similar to equilibrium wetting, and that active wetting transitions retain all the salient characteristics of equilibrium critical wetting – despite fundamental differences in underlying microscopic dynamics. Additionally, we uncover a ratchet mechanism on permeable barriers in active systems, and demonstrate that this gives rise to steady-state currents and a novel transition pathway in active wetting. Our results provide an intrinsically nonequilibrium framework in which to study active wetting, and precisely demonstrate the connection to equilibrium wetting – while clarifying how differences in microscopic dynamics give rise to novel macroscopic behaviour.

## I. INTRODUCTION

Active matter comprises a broad class of self-propelled particles, which consume energy at a local scale to produce directed motion. Such particles are extremely common in microbiological and ecological contexts, spanning length scales from microns to meters and involving particle numbers from dozens to millions [1–3]. Examples include swimming bacteria [4–6], flocking birds [7, 8], and cytoskeletal networks [2, 9] – as well as synthetic cases such as Janus particles [10] and robotic swarms [11].

The continuous consumption of energy drives active particles out of equilibrium, leading to a diverse range of emergent collective behaviours. For example, active particles undergo motility-induced phase separation (MIPS) into dense (liquid) and dilute (vapour) phases due to the interplay between volume exclusion and self-propulsion, even in the absence of explicitly attractive interactions [12, 13]. It is expected that collective behaviour in active systems should show some degree of independence of the microscopic details of particle interactions [2, 14], so simple particle-level [15–17] or field-theoretical [13, 18, 19] models of active matter are natural settings for studying their emergent behaviours.

A distinguishing feature of active systems, compared to their passive counterparts, is the outsized influence of boundaries. Non-local effects arising from steady state currents, as well as smaller typical system sizes, mean that boundaries play a much more central role in determining the collective behaviour of active matter than in the passive case. Indeed, recent studies have shown that boundaries can regulate transport, transfer energy

between length scales, and create or destroy large-scale structure [3, 20–29].

Perhaps the most prominent boundary-driven effect is the accumulation of active particles on repulsive barriers. Experiments and simulations have shown that the self-propulsion of active particles results a layer of density on any repulsive wall or barrier [30–40]; this behaviour is reminiscent of the wetting of surfaces in equilibrium [41–44], and so the phenomenon has become known as active wetting. Surface-driven accumulation is not just a theoretical prediction – experiments have implicated active wetting in a wide variety of biological processes [45, 46], including biofilm formation [47–51], epithelial tissue organisation [52, 53], and cytoskeletal movement [54].

Despite its outsized role in active systems, and biological relevance, the physics of active wetting remains poorly understood – complex interfacial phenomena and non-local effects mean that even basic results of equilibrium wetting theory are not necessarily applicable to the active case [29, 31, 55–58]. In particular, the phenomenology of active matter cannot be rationalised in terms of a single effective surface tension [13, 56]. An intrinsically nonequilibrium framework is therefore required to understand, and harness, these boundary-driven phenomena.

In this work, we study active wetting via a new approach, by analysing a lattice model of self-propelled particles, whose large-scale (hydrodynamic) behaviour can be derived exactly [59–61], and is governed by deterministic equations. A consequence of the hydrodynamic limit as taken here is that the large-scale behaviour of our model is not affected by fluctuation corrections (in the sense of the renormalisation group). This leads to critical behaviour of mean-field type. Nevertheless, we explain below that our results provide generic insights

---

\* Corresponding author: njbg2@cam.ac.uk (he/him)

for active wetting.

The hydrodynamic framework – which has also provided important recent insights in other types of active system [62, 63] – allows us to use precise mathematical analysis techniques familiar from field theories, while retaining a direct connection to microscopic behaviour<sup>1</sup>. This means we can identify subtle yet physically significant effects, which may be obscured in particle-level studies [30] by the confounding role of noise.

We study wetting on a penetrable barrier in a periodic geometry, similar to the one studied in [30]; this is analogous to a slit geometry conventionally used to investigate equilibrium wetting [64]. Our deterministic equations result in a system which remains translationally symmetric in the direction(s) parallel to the wall, and so we study one-dimensional (1d) profiles – although our model admits a general and exact description even in higher dimensions.

Using this framework, we uncover two key results. The first is that active wetting states appear remarkably similar to their equilibrium counterparts, despite fundamental differences in their microscopic dynamics. Not only can we show that density profiles in a slit geometry are analogous to equilibrium wetting states, but we also demonstrate that the transition between full and partial wetting states retains all the salient characteristics of a critical wetting transition, in which the density profile changes continuously on approaching the wetting transition. Despite these similarities, our second key result is that permeable barriers induce a ratchet effect in active systems – this leads to a steady-state current in the partially-wet state, and a novel pathway for the full-to-partial wetting transition, which would be forbidden for passive fluids. Taken together, these results rigorously connect equilibrium and active wetting, while clarifying how nonequilibrium microscopic dynamics gives rise to novel macroscopic behaviour.

The remainder of this paper is structured as follows: Sec. II gives a short review of the equilibrium theory of wetting and defines the model studied here. Sec. III presents the surface phase diagram to describe steady-state wetting, and characterises the wetting states and their transition. Sec. IV then analyses the dynamical pathway of transitions between the fully- and partially-wet states. We first qualitatively characterise the dynamical mechanism, and then derive a minimal model to recreate this dynamics and understand the origins of the novel pathway. Sec. V summarises our conclusions, including a discussion of the results and their implications.

<sup>1</sup> One aspect that aids this connection is that particle density and orientation fields both appear in the hydrodynamic equations; this differs from most active field theories, which take the hydrodynamic limit in a different way that eliminates orientational dynamics but retains diffusive noise.

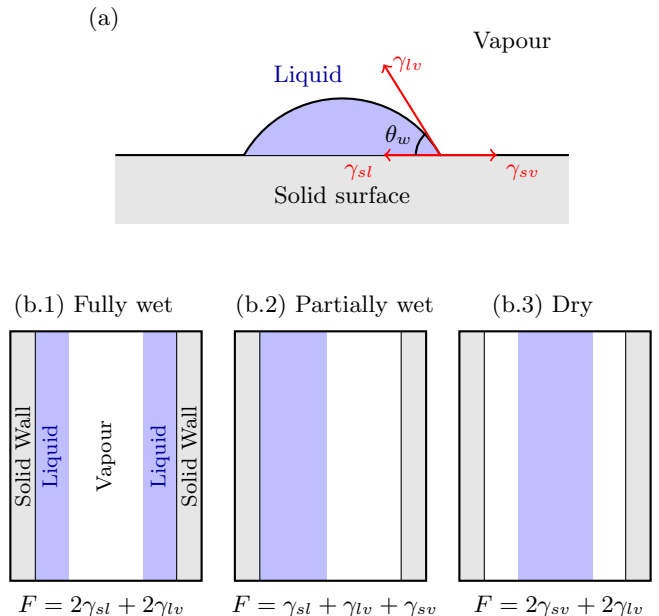


FIG. 1. (a) Diagram of equilibrium wetting on a solid surface. A liquid droplet rests on the solid in coexistence with the vapour phase, forming a contact angle  $\theta_w$ . The interfacial tensions  $\gamma_{sl}$ ,  $\gamma_{sv}$ , and  $\gamma_{lv}$  correspond to solid-liquid, solid-vapour, and liquid-vapour interfaces, respectively. (b) Schematic of wetting states in a slit geometry. (b.1) Fully wet: macroscopic liquid films coat both walls. (b.2) Partially wet: a macroscopic liquid film forms on one side. (b.3) Dry: no liquid adsorption at the walls.

## II. BACKGROUND & MODEL

### A. Equilibrium theory of wetting

Wetting describes the equilibrium behaviour of a fluid with coexisting liquid and vapour phases when it comes into contact with an attractive solid wall [41–44, 64]. The liquid typically forms droplets on the wall, characterised by a contact angle  $\theta_w$  (see Figure 1(a)). This contact angle can be calculated from the interfacial tensions between the liquid, vapour, and solid phases, and is given by Young's equation [41]

$$\cos(\theta_w) = \frac{\gamma_{sv} - \gamma_{sl}}{\gamma_{lv}}, \quad (1)$$

where  $\gamma_{lv}$ ,  $\gamma_{sv}$ , and  $\gamma_{sl}$  denote the liquid-vapour, solid-vapour, and solid-liquid interfacial tensions respectively. Young's equation can be derived either mechanically, by considering the balance of forces at the contact line [41], or statistically, via the variational minimisation of a free energy [65]. These perspectives are equivalent because the system is at equilibrium.

When  $\theta_w \in (0, \pi)$ , the liquid forms a droplet on the wall; this is called partial wetting. A wetting transition occurs when the contact angle  $\theta_w$  vanishes, and the liquid spreads across the wall to form a macroscopic film; this

state with  $\theta_w = 0$  is called full wetting. A drying transition occurs as  $\theta_w$  approaches  $\pi$  and the droplet pinches off from the wall.

Wetting is often studied in the context of a fluid in a slit geometry [30, 41, 64], where the fluid is confined between two parallel walls, separated by a macroscopic distance  $L$ . The system is assumed to be translationally symmetric in the direction(s) parallel to the walls; the total fluid mass, and other control parameters, are chosen such that both a bulk liquid and bulk vapour phase coexist. This allows for three possible wetting states (see Figure 1(b)):

- (i) *Fully wet*: The fluid forms a macroscopic liquid layer on both walls with a vapour bulk between them, such that the total energy per unit (transverse) area is  $2\gamma_{sl} + 2\gamma_{lv}$ .
- (ii) *Partially wet*: The fluid forms a macroscopic liquid layer on one wall while the other remains dry, such that the total energy per unit area is  $\gamma_{sl} + \gamma_{lv} + \gamma_{sv}$ .
- (iii) *Dry/Unpinned*: Both walls are dry, and there is an unpinned liquid bulk between the walls such that the total energy per unit area is  $2\gamma_{sv} + 2\gamma_{lv}$ .

Comparing the energies, the transition from partial to full wetting in the slit geometry occurs at  $\gamma_{sv} = \gamma_{sl} + \gamma_{lv}$  which corresponds to  $\theta_w = 0$ , as for the droplet. The wetting (and drying) transitions in the slit and droplet geometry therefore correspond to the same physical transition. We emphasize that a wet wall is covered by a macroscopic liquid layer of thickness  $\zeta = \mathcal{O}(L)$ . For attractive walls, even a “dry” wall is typically coated by a microscopic film of fluid,  $\zeta = \mathcal{O}(1)$  [41].

Wetting transitions occur as some control parameter is varied (for example, the strength of an attractive interaction between fluid and wall); we denote this quantity here by  $\epsilon$ . It is useful to define a spreading factor  $S = \gamma_{sv} - \gamma_{sl} - \gamma_{lv}$  [41], which is equal to

$$S = \gamma_{lv}[\cos(\theta_w) - 1], \quad (2)$$

in the partially wet state, with  $S < 0$ . A wetting transition means that  $S \rightarrow 0^-$  as a control parameter  $\epsilon$  tends to a critical value  $\epsilon^*$ . These transitions come in two types: first-order wetting involves  $S \rightarrow 0$  with a finite slope,  $dS/d\epsilon \neq 0$ ; in this case the fluid film thickness  $\zeta$  (on the “dry” side) approaches a finite limit as  $S \rightarrow 0$  and then jumps to a macroscopic value  $\zeta = \mathcal{O}(L)$  only in the fully-wet state. Critical transitions have  $S \rightarrow 0$  and  $dS/d\epsilon \rightarrow 0$  together; this signals a continuous divergence of the thickness  $\zeta$ , see below.

Cahn [41, 42] showed that the equilibrium wetting transition of a fluid on a planar wall, or in the slit geometry, can be described at hydrodynamic level by a one-dimensional Cahn-Hilliard field theory for the fluid density  $\rho$ , with free energy

$$F[\rho] = \int_0^\infty \frac{\kappa}{2} (\nabla \rho)^2 + W(\rho) + f_w(\rho) \delta(x) dx, \quad (3)$$

where  $W(\rho)$  is a double-welled potential describing bulk phase separation. The free energy due to interaction with the wall (at  $x = 0$ ) is contained in the function  $f_w(\rho)$ , which can be expanded in a Taylor series as

$$f_w(\rho) = c_0 - c_1\rho + \frac{1}{2}c_2\rho^2 + \mathcal{O}(\rho^3). \quad (4)$$

Here  $c_1$  roughly corresponds to the attractive interactions between the wall and the fluid, and  $c_2$  to the effect of exclusion of fluid by the wall, resulting in the loss of attractive fluid-fluid interactions (see [41]). Taking the control parameter  $\epsilon = c_1$  (so that the wetting transition occurs on varying the attraction strength),  $\epsilon < \epsilon^*$  corresponds to partial wetting (weaker attraction) and  $\epsilon > \epsilon^*$  to full wetting.

The wetting transition in a slit geometry, where impenetrable walls are placed at  $x = 0, L$ , can then be characterised using a global asymmetry order parameter [30]

$$\mathcal{A}[\rho] = \frac{\int_0^L |\rho(x) - \rho(L-x)| dx}{2L(\bar{\rho} - \rho_v)}. \quad (5)$$

Here  $\mathcal{A} = 0$  characterises full wetting,  $\mathcal{A} > 0$  indicates partial wetting, and the normalisation is such that  $\mathcal{A} \in [0, 1]$ .

Minimising the free energy (3) results in an equilibrium theory of wetting with mean-field character (because the hydrodynamic approach neglects density fluctuations). This theory is summarised in Appendix A; both critical and first-order wetting are possible in the Cahn theory, with critical wetting observed if  $c_2$  is sufficiently large. Physically, this corresponds to the scenario where the effect of the wall in preventing attractive interactions between fluid particles is large. For later convenience, we identify the main features of critical wetting, which differ from the first-order case. First, the film thickness on the dry wall diverges continuously at the wetting transition, as

$$\zeta \sim \log \frac{1}{\epsilon^* - \epsilon}, \quad \epsilon < \epsilon^*. \quad (6)$$

Second, the asymmetry parameter vanishes continuously as full wetting is approached (exhibiting a pitchfork bifurcation with a characteristic exponent of  $1/2$ ):

$$\mathcal{A} = \begin{cases} \alpha(\epsilon^* - \epsilon)^{1/2}, & \epsilon < \epsilon^*, \\ 0, & \epsilon \geq \epsilon^*, \end{cases} \quad (7)$$

where  $\alpha$  is a proportionality constant. Third, there are no metastable states so one does not expect hysteresis as  $\epsilon$  passes through  $\epsilon^*$ .

Density Functional Theory (DFT) models, renormalisation group calculations, and Monte-Carlo simulations [43, 64, 66–68] have been used to extend the equilibrium wetting theory to more precisely connect to particle-level descriptions, and incorporate the effects of fluctuations arising from thermal noise. The resulting picture is complex, with the order of wetting transitions depending sensitively on the dimensions of the system, as well as the

details of the fluid-fluid and wall-fluid interactions. In general, critical wetting appears to be the more common scenario in two dimensions ( $d = 2$ ).

## B. Active lattice gas model

### 1. Exact hydrodynamic description

We study the active lattice gas introduced in [60], which involves particles that move on an  $N \times N$  square lattice, with at most one particle per site, and an external potential  $V$ . We embed the lattice into a domain of size  $L \times L$ , so that the lattice spacing is  $L/N$ . The hydrodynamic limit is  $N \rightarrow \infty$  at fixed  $L$ . Each particle  $i$  is endowed with a position  $\mathbf{x}_i$  and an orientation vector  $\mathbf{e}(\theta_i) = (\cos(\theta_i), \sin(\theta_i))^T$ . It hops from  $\mathbf{x}_i$  to a vacant neighbouring site  $\mathbf{x}_i + \mathbf{u}$  with rate

$$w_i(\mathbf{u}) = N^2 \left\{ D_E + \frac{v_0}{2} \mathbf{u} \cdot \mathbf{e}(\theta_i) + \frac{V(\mathbf{x}_i) - V(\mathbf{x}_i + \mathbf{u})}{2} \right\}. \quad (8)$$

(Note that  $|\mathbf{u}| = L/N$  is small in the hydrodynamic limit.) Each angle  $\theta_i$  undergoes Brownian motion on the unit circle with orientational diffusion constant  $D_O$ . The only interactions between particles are excluded volume interactions. On taking the hydrodynamic limit, it is important that particles' movement rates are chosen to have a non-trivial  $N$ -dependence, so that both diffusive and self-propelled contributions remain comparable as  $N \rightarrow \infty$ . This feature enables the exact calculation; it involves a limit of fast diffusion that suppresses fluctuations so that the resulting system is mean-field type, similar to the Cahn theory. These dynamics also exclude inertial effects; while inertia is known to influence wetting behaviour in active systems [40], this is not considered here.

The system is described in the hydrodynamic limit by a phase space density  $f(\mathbf{x}, \theta, t)$  for particles with spatial position  $\mathbf{x}$  and orientation  $\theta$  at time  $t$ . The spatial density  $\rho$  and polarization  $\mathbf{p}$  of the particles are then

$$\rho(\mathbf{x}, t) = \int_0^{2\pi} f(\mathbf{x}, \theta, t) d\theta, \quad (9)$$

$$\mathbf{p}(\mathbf{x}, t) = \int_0^{2\pi} f(\mathbf{x}, \theta, t) \mathbf{e}(\theta) d\theta. \quad (10)$$

(Note that  $\rho(\mathbf{x}, t) \in [0, 1]$ : this quantity represents the average occupancy of sites in the vicinity of position  $\mathbf{x}$ . The number density of particles is diverging proportional to  $N^2$  in the hydrodynamic limit.) The deterministic evolution of  $f$  is given by:

$$\frac{\partial f}{\partial t} = -D_E \nabla \cdot \mathbf{J}_{\text{diff}} - v_0 \nabla \cdot \mathbf{J}_{\text{activity}} + D_O \partial_\theta^2 f, \quad (11)$$

where

$$\mathbf{J}_{\text{diff}} = -d_s(\rho) \nabla f - f \mathcal{D}(\rho) \nabla \rho - f(1 - \rho) \nabla V, \quad (12)$$

$$\mathbf{J}_{\text{activity}} = (\mathcal{D}(\rho) - 1) f \mathbf{p} + \mathbf{e}_\theta d_s(\rho) f. \quad (13)$$

We define  $d_s(\rho)$  as the diffusion constant in a symmetric exclusion process at density  $\rho$  (see below), and we take  $\mathcal{D}(\rho) = [1 - d_s(\rho)]/\rho$  for ease of writing. The first two terms in  $\mathbf{J}_{\text{diff}}$  were derived in [60], subject to the unknown function  $d_s(\rho)$ , while the final term is a modification introduced by the presence of an external potential, see Appendix B 1. It was shown in [69] that the self-diffusion coefficient can be accurately approximated as:

$$d_s(\rho) = (1 - \rho) \left( 1 - \alpha \rho + \frac{\alpha(2\alpha - 1)}{2\alpha + 1} \rho^2 \right), \quad (14)$$

where  $\alpha = \frac{\pi}{2} - 1$ . This formula for  $d_s$  is exact in both the low- and high-density limits and gives accurate approximations for all densities. We will use it below whenever an explicit form for  $d_s(\rho)$  is required. We identify two length scales associated with the particle dynamics:

$$l_p = \frac{v_0}{D_O}, \quad l_D = \sqrt{\frac{D_E}{D_O}}, \quad (15)$$

where  $l_p$  corresponds to the typical distance a particle moves before changing direction, and  $l_D$  sets the width of liquid-vapour interfaces.

It is convenient to rescale time as  $t \rightarrow D_O t$ , and space as  $x \rightarrow \frac{x}{l_D}$ , such that both are made dimensionless. The hydrodynamic equation (11) becomes

$$\frac{\partial f}{\partial t} = -\nabla \cdot \mathbf{J}_{\text{diff}} - \text{Pe} \nabla \cdot \mathbf{J}_{\text{activity}} + \partial_\theta^2 f, \quad (16)$$

where

$$\text{Pe} = \frac{l_p}{l_D} = \frac{v_0}{\sqrt{D_E D_O}} \quad (17)$$

is the Péclet number, describing the strength of self-propulsion. We work with these rescaled space and time variables throughout the following results.

The active lattice gas exhibits motility-induced phase separation (MIPS), arising from the interplay between the self-propulsion of the particles and the excluded volume interactions between them [12, 14, 60]. The spinodal curve was computed in [60]. The binodal can be computed by simulating the hydrodynamic equation (11) – see Appendix C 2. The resulting phase diagram is shown in Figure 2.

### 2. System geometry and wall/barrier potential

Following [30], we study a two-dimensional system with periodic boundary conditions, and a penetrable wall (or “barrier”) located at  $x = 0$ . In the limit of large barrier height, this becomes the slit geometry of Figure 1(b). Hard walls are typically fully wet in active systems [30, 32], due to the generic accumulation of active particles near solid barriers [23, 24, 33]. Partial wetting states have been observed in active systems, either with soft walls [55], or using penetrable barriers [30, 39]. We

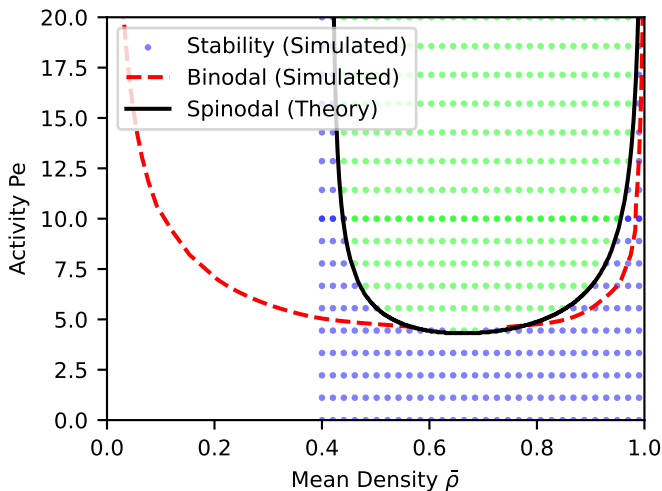


FIG. 2. Phase diagram of the active lattice gas. The binodal (coexistence curve) is obtained by simulating at (11) and characterising the phase-separated steady-states. The spinodal is obtained from [60], it is compared with numerical stability results for (11) starting from weakly perturbed homogeneous states (coloured points, no data shown for  $\bar{\rho} < 0.4$ ). The critical point where the spinodal and binodal curves intersect is  $(\bar{\rho}_{\text{crit}}, \text{Pe}_{\text{crit}}) = (0.659, 4.33)$ . As is usual for active phase separation [13], these binodals (dashed curves) do not depend on the value  $\bar{\rho}$  so long as it lies between them. See Appendix C 2 for further details.

choose a barrier whose softness and penetrability scale together, in order to access a transition between full- and partial-wetting states. Periodic boundary conditions are used to avoid introducing any additional confining boundaries.

Since the governing PDEs are deterministic and the initial condition is chosen to be translationally invariant along the direction parallel to the walls, the probability density  $f(\mathbf{x}, \theta, t)$  only depends on the component  $x$  of the position  $\mathbf{x}$  perpendicular to the barrier. Hence, we consider 1d density profiles  $f(x, \theta, t)$  in the following, although we emphasize that the underlying lattice model is 2d and can easily be generalised to higher dimensions [60, 61]. (Indeed, it is not possible to have orientational diffusion at fixed propulsion speed  $v_0$  in one spatial dimension.) We choose a system with domain size  $L$  in the  $x$ -direction.

The barrier potential is taken as in [30]:

$$V(x) = \begin{cases} 0 & \text{if } |x| \geq w_b, \\ \epsilon \left[ \cos\left(\frac{\pi x}{w_b}\right) + 1 \right] & \text{if } |x| < w_b, \end{cases} \quad (18)$$

so the strength of the barrier potential is a dimensionless parameter  $\epsilon$ ; its half-width  $w_b$  is fixed throughout as  $w_b = l_D/2$ . The final (dimensionless) control parameter, alongside the barrier strength  $\epsilon$  and the activity level  $\text{Pe}$ , is the (conserved) total density

$$\bar{\rho} \equiv \frac{1}{L} \int_0^L \rho(x) dx \quad (19)$$

For later convenience, we define the associated probability current in the joint position/orientation phase space as

$$\mathcal{J} = \begin{pmatrix} J_x \\ -D_0 \partial_\theta f \end{pmatrix}, \quad (20)$$

where  $J_x$  is the  $x$ -component of the vector  $\mathbf{J} = D_E \mathbf{J}_{\text{diff}} + v_0 \mathbf{J}_{\text{act}}$ . The probability current  $\mathcal{J}$  is a function of  $(x, \theta, t)$  and the hydrodynamic equation (11) for 1d profiles becomes  $\partial_t f = -(\partial_x, \partial_\theta) \mathcal{J}$  in this notation.

In summary, our system has five control parameters. Two intensive quantities, the Peclet number  $\text{Pe}$  and mean density  $\bar{\rho}$ , control particle behaviour. The barrier height is  $\epsilon$ , and its width  $w_D$  is set to  $l_D/2$  throughout. Finally, the (reduced, dimensionless) system size is  $\ell_s = L/l_D$ .

### III. RESULTS – STEADY-STATE

We access the wetting transition by varying the self-propulsion  $\text{Pe}$  and the barrier height  $\epsilon$ . We fix the total density at its critical value  $\bar{\rho} = 0.659$ , identified via linear stability analysis (see Appendix C and [60]); we mostly take  $\text{Pe}$  above its critical value, in which case results depend weakly on  $\bar{\rho}$ , as long as it remains inside the spinodal (recall Fig. 2). Repeating the analysis at different values of  $\bar{\rho}$  inside the spinodal leads only to small movements of the transition lines, instead of changes to the structure of the phase diagram. We choose different values of the reduced system size  $\ell_s$  according to the context, but these are always large enough such that we recover bulk liquid and vapour phases, far from interfaces and the barrier. For the numerical solution of (11), we discretise  $f$  onto a grid of size  $N_x \times N_\theta$  (see Appendix C for the detailed procedure). We take  $(N_x, N_\theta) = (200, 30)$  unless otherwise stated.

#### A. Full and partial wetting

Figure 3(a) shows the surface phase diagram, for a range of  $\epsilon, \text{Pe}$ . To obtain this, we initialise the system in a homogeneous state

$$f(x, \theta, 0) = \frac{\bar{\rho}_{\text{crit}}}{2\pi} + \delta f, \quad (21)$$

where  $\delta f \sim 10^{-4}$  is a small perturbation, uncorrelated in space. The system is then evolved to a final time  $t_f = 200$ , and states/transition lines are classified according to the routine described in Appendix C, based on an extrapolation to the large time limit. We identify four distinct steady-states, analogous to the states found in equilibrium wetting. These are labelled fully-wet, partially-wet, unpinned, and homogeneous. They are illustrated in Figures 3(b–e). The fully-wet state is symmetric, with liquid layers of equal width on either side of the barrier. The partially-wet state has a macroscopic liquid layer on one side of the barrier; the other

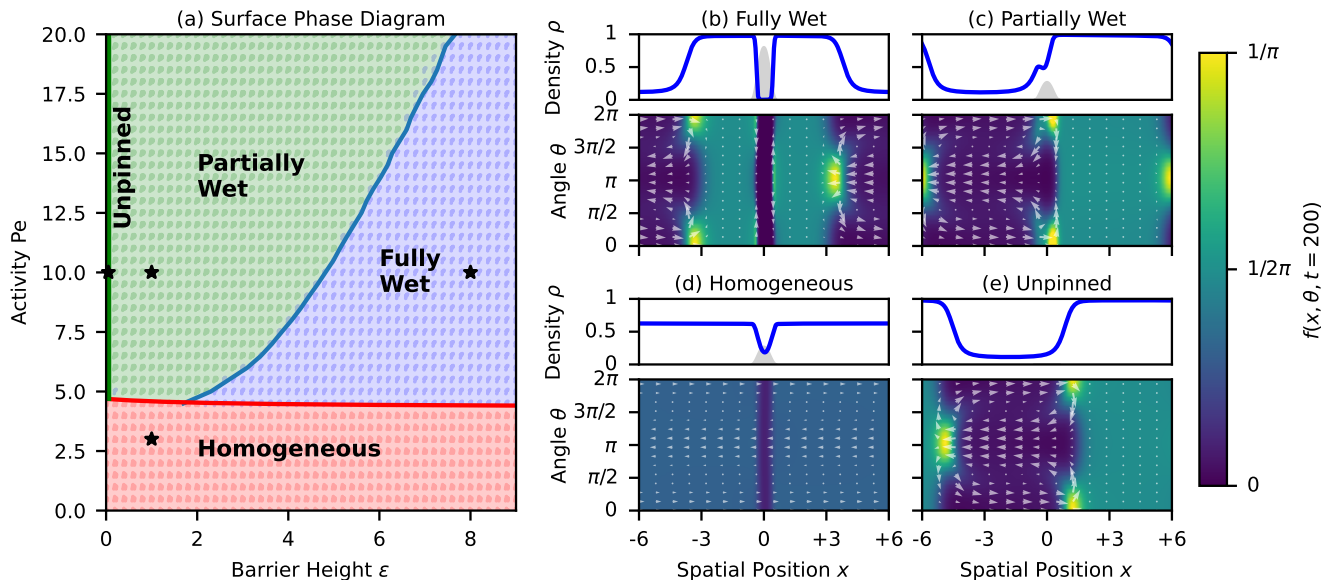


FIG. 3. Wetting of a barrier by the active lattice gas. (a) Surface phase diagram in the  $(\epsilon, Pe)$  plane. Each point represents a numerical solution (simulation) of the hydrodynamic equation, whose final state is classified with the routine described in Appendix C, which also explains the estimation of the phase boundaries. The red line is the onset of MIPS; the blue line is the wetting transition; the green line represents unpinning of the liquid at  $\epsilon = 0$ . The structure of the wetting phase diagram does not depend on  $\bar{\rho}$ , as long as it remains inside the spinodal. (b-e) Snapshots of the steady-state densities  $f(x, \theta)$  and  $\rho(x)$  for the starred points shown in the phase diagram, which illustrate the four phases. The upper plots show the density profile  $\rho(x)$ , and the potential  $V(x)$ ; the lower plots show  $f(x, \theta)$  (colour) and  $\mathcal{J}(x, \theta)$  (arrows – scaled proportionally to  $\mathcal{J}^{1/4}$ ).

side is coated by a thin film of finite width  $\zeta$ , see also below. The unpinned state is defined by the liquid bulk detaching from the barrier entirely; this is only observed when the barrier is removed completely ( $\epsilon = 0$ ). This may be expected since any barrier breaks the translational symmetry, which is sufficient to localise the liquid droplet (we emphasize that these hydrodynamic equations are deterministic, so there is no noise to drive the liquid away from the barrier). The homogeneous state occurs for  $Pe < Pe^* = 4.33$  where the system does not phase separate and wetting phenomenology is not expected.

The steady-state results for  $f(x, \theta, t)$  are consistent with expectations for active systems [22], in that the orientations of the active particles are isotropic in bulk phases but develop anisotropic structure at the liquid-vapour interface and at the barrier. One observes significant probability currents  $\mathcal{J}(x, \theta)$  in steady-state; these are divergence-free (consistent with  $\partial f / \partial t = 0$ ) and arise from particles' self-propulsion.

The boundary between full and partial wetting in Figure 3(a) is obtained numerically by testing the linear stability of the fully-wet state. There is no metastability at this transition (see Section III B below), so this procedure allows accurate determination of the phase boundary based on short simulations. Figure 3(a) shows that the critical barrier height  $\epsilon^*$  above which full wetting occurs is increasing with the activity  $Pe$ . This is expected: at higher activity, particles exert a stronger driving force

and can more easily overcome the barrier. The barrier thus becomes effectively softer and more permeable, favouring partial wetting (recall Section II B 2).

## B. The wetting transition is critical

We now examine in detail the wetting transition, which separates fully and partially-wet states. We find that this transition bears all the characteristics of an equilibrium critical wetting transition (recall Sec. II A). The control parameter for active wetting is the barrier height  $\epsilon$ . We write  $\epsilon^*(Pe)$  for the ( $Pe$ -dependent) location of the transition. Figure 4 shows results for  $Pe = 10$ . We verified that these qualitative features are robust across a range of  $Pe > Pe^*$ , and for other values of  $\bar{\rho}$  inside the spinodal.

(a) *Continuous divergence of the liquid film width.* Recall from (6) that for critical wetting, the dry wall in a partially-wet state carries a thin liquid film whose width  $\zeta$  diverges continuously at the wetting transition. Evidence for such a divergence is shown in Figure 4(a), which may be contrasted with a first-order wetting scenario, where  $\zeta$  would have a finite limit as the transition is approached. The nature of the divergence is logarithmic in equilibrium [41, 42] but we are not aware of any theoretical predictions for active (non-equilibrium) systems.

(b) *Square-root divergence of the asymmetry.* The fully-wet state is symmetric under reflection about  $x = 0$  so  $\mathcal{A} = 0$ , while the partially-wet state has  $\mathcal{A} > 0$ . Re-

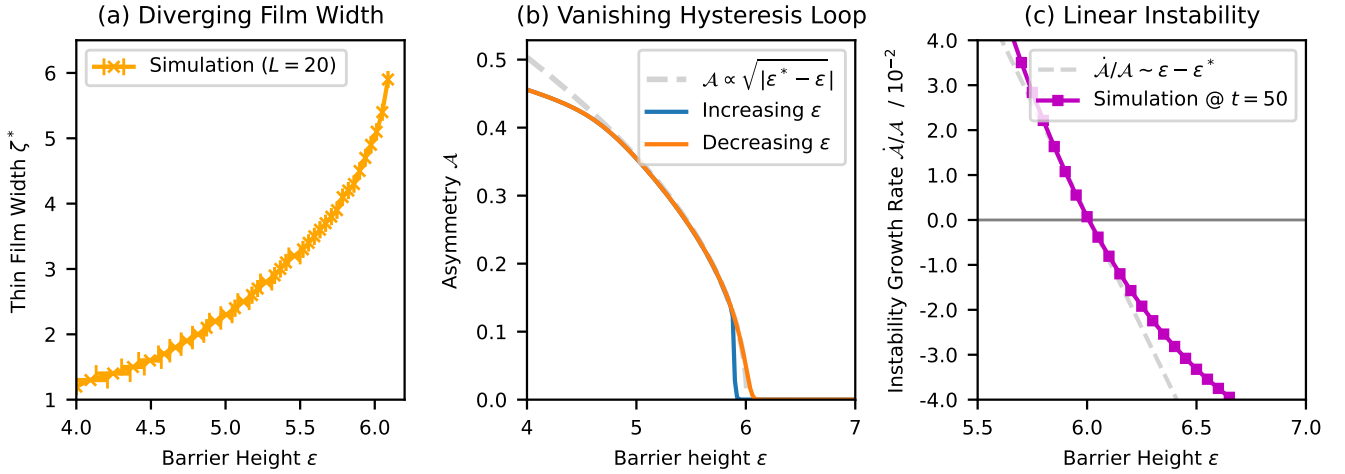


FIG. 4. The wetting transition between fully- and partially-wet states is critical. All plots are at  $Pe = 10$ . (a) The width of the liquid film on the “dry” wall, estimated by measuring the distance between the inflection points of  $\rho$  at the liquid-boundary and liquid-vapour interfaces. This increases as the transition is approached. Results are shown for a system of size  $\ell_s = 20$ , so maximum width of (symmetric) liquid layers is approximately 6.3 (using the lever rule). For an infinite system we expect  $\zeta$  to diverge at  $\epsilon = \epsilon^*$ . (b) Asymmetry  $\mathcal{A}$  as a function of  $\epsilon$ , scanning both up (blue) and down (orange), to check for hysteresis. The total scan time is  $T_{\text{tot}} = 2 \times 10^5$ ; we use a system size  $\ell_s = 5$ , smaller than in (a), such that the scan is quasi-static and the behaviour of  $\mathcal{A}$  is not too sharp (see Appendix A). The dashed grey line is a fit to (7). We estimate  $\epsilon^* \approx 6.01$ . The hysteresis loop is observed to shrink as the scan time is increased. (c) Linear stability of the fully-wet state with the same parameters. We plot the exponential growth rate of the asymmetry  $\dot{\mathcal{A}}/\mathcal{A}$  as a function of barrier height  $\epsilon$ . Positive values correspond to partial wetting (the fully-wet state is unstable), and we estimate  $\epsilon^* \simeq 6.01$  from a linear fit. The growth rate is measured at  $t = 50$ , when asymmetry growth is approximately linear and  $\mathcal{A}$  remains small.

call from (7) that for critical equilibrium wetting, the asymmetry is predicted to vanish as  $(\epsilon^* - \epsilon)^{1/2}$  on approaching the transition. This behaviour is illustrated in Figure 4(b); the exponent  $1/2$  appears robust even out of equilibrium, as may be expected generically for pitchfork bifurcations<sup>2</sup>.

(c) *Vanishing hysteresis loop.* Figure 4(b) also contrasts the behaviour on increasing and reducing  $\epsilon$  across the transition. There is no evidence for metastable states (neither partially- nor fully-wet). This is the expected behaviour for critical wetting. At a first-order transition, we would expect these noiseless hydrodynamic equations to support a finite hysteresis loop, even if  $\epsilon$  is varied quasi-statically.

(d) *Linear instability of the fully-wet state.* Another characteristic feature of critical wetting, which provides further confirmation of the absence of metastability, is that the fully-wet state becomes linearly unstable to density perturbations exactly at  $\epsilon^*$ . This means that

$$\frac{d}{dt} \ln(\mathcal{A}(t)) = \lambda(\epsilon^* - \epsilon) + \mathcal{O}((\epsilon^* - \epsilon)^2). \quad (22)$$

This behaviour is shown numerically in Fig. 4(c): we apply a small perturbation to the fully-wet state and measure the asymmetry as a function of time. As expected, we see linear instability of the fully-wet state above the critical barrier height  $\epsilon^*$ .

The transition between fully- and partially-wet states therefore bears all the hallmark characteristics of a critical wetting transition, and so we conclude that this active wetting transition is critical. In the Cahn theory of equilibrium wetting, critical wetting occurs when the effect of the barrier in preventing attractive interactions between fluid particles is significant (i.e.  $c_2$  is large, recall Section II A and Appendix A). In the active wetting scenario, these attractions are indeed strongly suppressed near the barrier; the large polarisation  $\mathbf{p}$  near the barrier means that active particles near the barrier are locally aligned. Since effective attractive interactions in MIPS arise due to collisions between oppositely aligned particles [12], the barrier inhibits the attractive fluid-fluid interactions dramatically – in the large  $Pe$  limit, we expect this inhibitive effect to become absolute. This offers a physical explanation for the observation of critical wetting in the active system.

<sup>2</sup> This behaviour is reminiscent of that observed in a system of two columns containing driven granular gases, separated by a permeable barrier, which exhibits a pitchfork bifurcation in the system’s asymmetry – see [70].

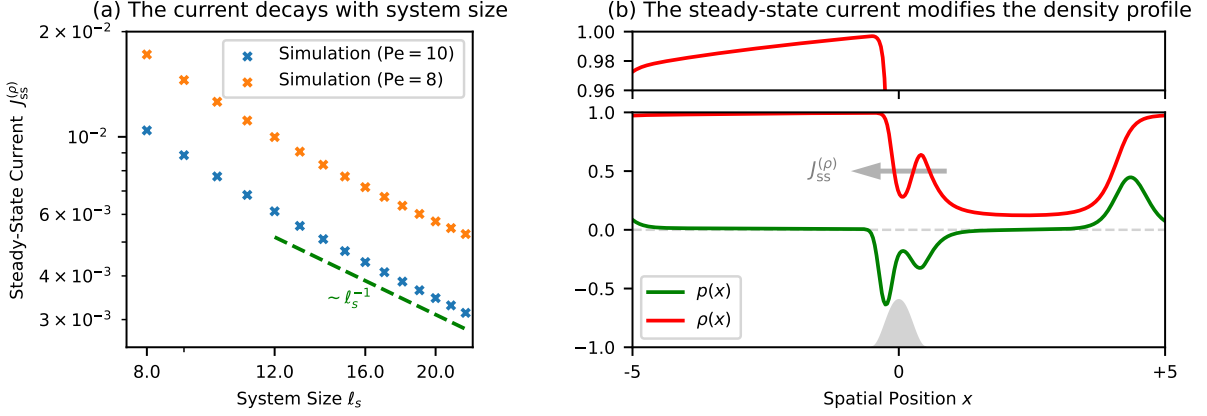


FIG. 5. Illustration of steady-state current in the partially-wet state. (a) Steady-state current as a function of system size, scaling as  $J_{ss}^{(\rho)} \propto 1/\ell_s$  for large systems. These results are for simulations with spatial resolution  $N_x = 200$ ; some points were repeated with  $N_x = 500$ , and the current changes by less than 2%. (b) Steady-state density  $\rho(x)$  and polarisation  $p_x(x)$ , for  $\epsilon = 2.0$ ,  $Pe = 10$ ,  $\ell_s = 10$ . The barrier profile and current direction are shown in light grey. Density accumulates in the liquid bulk and on the dry side of the barrier. Regions of net polarisation are visible pointing into the liquid bulk, and pointing into the barrier on the dry side. The top panel magnifies the density profile in the liquid phase, which has a finite gradient, facilitating a diffusive current.

### C. Ratchet current (partially-wet state)

Although the steady-states discussed thus far are analogous to equilibrium wetting, we also see striking non-equilibrium effects. In particular, the partially-wet state exhibits a steady-state density current, which flows around the periodic boundary conditions; such time-reversal symmetry breaking would be forbidden in equilibrium.

For a simple notation, we denote the density current by  $\mathbf{J}^{(\rho)}(\mathbf{x})$ , such that the dynamics of the conserved density field is given by  $\partial_t \rho(\mathbf{x}) = -\nabla \cdot \mathbf{J}^{(\rho)}(\mathbf{x})$ . As the system has only one non-uniform direction  $x$ , we work with the  $x$ -component of this quantity  $J^{(\rho)}(x)$ . We can obtain an expression for the density current by integrating (16) over the particles' orientations  $\theta$ , which yields:

$$J^{(\rho)}(x) = -(\partial_x \rho + \rho(1 - \rho)\partial_x V) + Pe(1 - \rho)p_x \quad (23)$$

(see Appendix B 2 for further details). Noting that this (divergence-free) current must be a constant in steady-state, and using the steady-state identity  $\int_0^{\ell_s} \mathbf{p}(x) dx = \mathbf{0}$ , leads to:

$$J_{ss}^{(\rho)} = -M[\rho] \int_0^{\ell_s} \rho(x) \frac{\partial V}{\partial x} dx, \quad (24)$$

where

$$M[\rho] = \frac{1}{\int_0^{\ell_s} [1 - \rho(x)]^{-1} dx} \quad (25)$$

plays the role of a mobility, and is strictly positive.

Since we consider a parity-symmetric barrier  $V(x) = V(-x)$ , a steady-state current can only arise if the density profile breaks parity symmetry about the barrier,

i.e. in the partially-wet state. Noting that  $M[\rho] > 0$  one also sees that the current in (24) is positive in cases where density is larger on the right side of the barrier, and negative where density is larger on the left. Current therefore flows from the dry side of the barrier to the wet side. This is consistent with a genuine ratchet effect, as opposed to an enhancement of the diffusion current from high- to low-density regions.

For large systems  $\ell_s \rightarrow \infty$ , one sees from (25) that the mobility tends to zero as  $M \sim \ell_s^{-1}$ ; the integrand in (24) is non-zero only for  $|x| < w_d$ , so the integral remains of order unity. Hence the current is suppressed in large systems as

$$J_{ss}^{(\rho)} \sim \ell_s^{-1}. \quad (26)$$

This scaling arises because the ratchet acts as a localized driving force, while the friction is distributed across all particles.

The system-size dependence of  $J_{ss}^{(\rho)}$ , as well as its direction, are illustrated in Figure 5. We see the expected scaling of the current in large systems, and current flows in the predicted direction. The spatial variance of the current is observed to be  $\sim 10^{-11}$  relative to its absolute value – this confirms that the current is indeed uniform. Simulations reveal a further consequence of this steady-state current; the density profile in the partially-wet state is modified, with the liquid droplet developing a linear density gradient across its bulk, as seen in Figure 5(b). This gradient enables diffusive transport of particles, sustaining the steady-state current throughout the system. Such gradients are absent in passive wetting, where the bulk density must remain uniform away from the barrier. Its presence here is a non-local effect of the barrier, mediated by the active dynamics.

The described current is consistent with the fact that asymmetric barriers, accompanied by the breaking of time-reversal symmetry due to self-propulsion, lead generically to currents via a ratchet effect in active systems [22, 26–28]. While the system here has (spatial) inversion symmetry, this is spontaneously broken in the partial wetting state. The direction of the ratchet current is therefore random, determined by which side of the barrier is wet and which is dry.

To summarise, our analysis of the steady-state solutions of (16) has revealed a rich phenomenology. We have demonstrated that solutions of the hydrodynamic equations closely resemble equilibrium wetting states, despite fundamental differences in microscopic dynamics. Additionally, we have shown that the wetting transition retains the key characteristics of critical wetting in passive fluids. Despite these similarities, we also see classically forbidden phenomena – the partial wetting solution exhibits a steady-state circulating current, driven by a ratchet effect on the barrier. In the following section, we investigate how this same ratchet effect dramatically reshapes the dynamical pathways between full and partial wetting.

#### IV. RESULTS – DYNAMICAL TRANSITIONS

Having discussed the steady-state behaviour of the system, we now turn to the dynamics of transitions between fully- and partially-wet states. While time-invariant wetting states reported above are analogous to those of equilibrium wetting, the dynamics of their transitions differ significantly. In particular, the transition pathway from the fully to the partially-wet state is driven by a ratchet mechanism at the barrier; as stated above, this is an intrinsically non-equilibrium effect, with no analogue in passive wetting. We first describe the dynamics of this transition, and then derive a minimal model to recreate the novel transition and elucidate its origins.

##### A. Non-equilibrium transition mechanism for the active lattice gas

We initialised the system in a fully-wet steady-state, after which we reduced the barrier strength  $\epsilon$  such that the stationary state becomes partially-wet. As noted above, this makes the fully-wet state linearly unstable, and an initial small density perturbation triggers a transition to the partially-wet state. Such a transition is illustrated in Figure 6(a,b).

The subsequent transition pathway unfolds in three distinct stages. First, the linear instability leads to a reduction in density on one side of the barrier, and the asymmetry grows exponentially:

$$\mathcal{A}(t) = A_1 e^{\lambda(\epsilon^* - \epsilon)t}, \quad (27)$$

recall (22).

Next, the liquid layer detaches from the barrier on the low-density side to form a droplet. This detached liquid droplet evaporates at an approximately constant rate, leading to a linear increase in asymmetry:

$$\mathcal{A}(t) \approx A_2 t. \quad (28)$$

Finally, the detached liquid droplet “bursts”<sup>3</sup>, redistributing its mass onto the barrier and the other liquid layer. After this redistributed mass is absorbed onto the liquid wetting layer<sup>4</sup>, the asymmetry saturates:

$$\mathcal{A}(t) = A_3. \quad (29)$$

An example of this process is shown in Figure 6(a). The approximate onset times of stages 1, 2, and 3 are  $t_1 = 0$ ,  $t_2 = 250$ , and  $t_3 = 650$  respectively. The corresponding behaviour of  $\mathcal{A}(t)$  is shown in Figure 6(b), where we observe exponential, then linear, and finally saturated growth. The “bursting” of the liquid droplet at time  $t \approx t_3$  appears as relatively fast changes in  $\mathcal{A}(t)$ . Although only a single example of this dynamical transition is shown, the same experiment was repeated across a range of  $\bar{\rho}$  and  $Pe$ , yielding transitions with the same dynamical stages.

The appearance of a vapour bulk between the liquid droplet and the barrier requires creation of a liquid-vapour interface and a vapour-wall interface, while a liquid-wall interface is removed. In equilibrium, this would have free energy cost per unit transverse area

$$\Delta F = \gamma_{lv} + \gamma_{sv} - \gamma_{sl}. \quad (30)$$

Recalling that the wetting transition takes place when  $\gamma_{sv} - \gamma_{sl} = \gamma_{lv}$  one sees that  $\Delta F \approx 2\gamma_{lv}$  close to the transition. A consistent equilibrium theory requires positive surface tension  $\gamma_{lv} > 0$  so this process would always cost free energy. Such processes are forbidden in hydrodynamic theories of equilibrium systems, for which the free energy is non-increasing. The observed pathway, occurring via the detachment of a liquid droplet, is therefore inaccessible for passive fluids.

In contrast, the mechanism of the reverse transition (from the partially-wet to the fully-wet state) resembles the translational instability found in equilibrium (recall Appendix A). This is illustrated in Figure 6(c) – the smaller liquid layer grows until it matches the width of the larger layer.

<sup>3</sup> This sudden behaviour occurs when the liquid droplet reaches a certain minimum size, and the overlap between the exponential tails of the liquid-vapour interfaces becomes significant, destroying bulk stability. Although fast compared to the initial evaporation, this process (and the subsequent redistribution of mass) remains sufficiently slow to be clearly resolved in the simulation.

<sup>4</sup> The absorption of the redistributed mass into the bulk liquid also appears fast, presumably due to the same mechanism as the fast bursting of the liquid droplet. However, this process remains much slower than the simulation timestep.

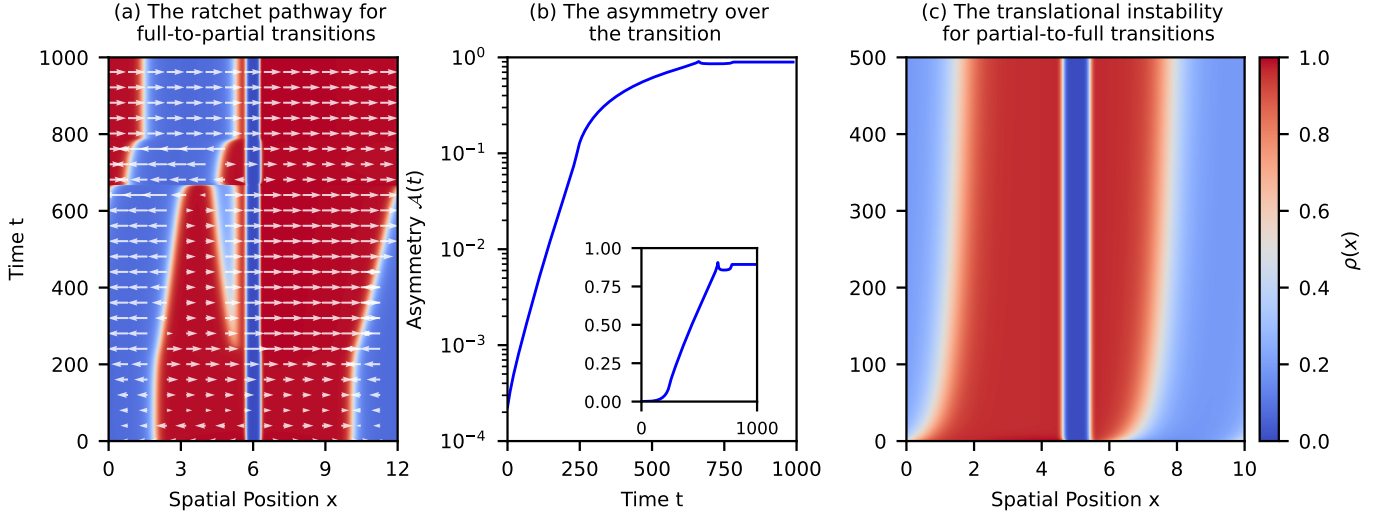


FIG. 6. Mechanism of the full-to-partial wetting transition, see the main text for detailed discussion. (a) The evolution of the density field  $\rho(x)$  (colour) and spatial current  $J_x$  (arrows – scaled proportionally to  $J^{1/4}$ ) during a full-to-partial wetting transition. The system is initialised in a fully-wet state, but  $\epsilon$  is chosen such that the ground state is partially-wet. (b) The asymmetry  $\mathcal{A}$  shows initial exponential growth followed by a linear increase, and then saturation. The inset shows the same data on a linear scale. (c) The evolution of the density field  $\rho(x)$  during a partial-to-full wetting transition. The same colour bar is used for (a,c).

## B. Minimal model for a ratchet-induced transition mechanism

Two inherently non-equilibrium effects have been described so far; a steady-state current in the partially-wet state, and a novel dynamical pathway from full- to partial-wetting. The first is clearly a consequence of the ratchet effect on the barrier (see (24)). To understand the origin of the novel dynamical pathway, we create a minimal model of the active system, which contains phase separating fields and a localised active ratchet – all other consequences of the barrier and self-propulsion are discarded in the minimal model. By demonstrating that this minimal model has a transition at non-zero ratchet strength between full- and partial-wetting, with the same novel pathway as the full dynamics, we show that the ratchet effect is primarily responsible for the novel dynamical pathway (instead of any other consequence of the barrier, e.g. excluded volume interactions).

### 1. Construction of the minimal model

To create such a minimal model, we start with the dynamics of the density field in the full model. The calculation is presented here in one spatial dimension, see Appendix D for the general case. Integrating (16) over the particles' orientations  $\theta$  yields:

$$\partial_t \rho(x) = -\partial_x [J^{(\rho)}(x)] \equiv -\partial_x [\mathcal{M}(\rho(x))\mathcal{F}(x)], \quad (31)$$

where  $\mathcal{M}(\rho) = 1 - \rho \geq 0$  plays the role of a mobility. The generalised force  $\mathcal{F}(x)$  can be split into two contributions:

$$\mathcal{F} = \overbrace{\partial_x \ln(1 - \rho)}^{\mathcal{F}_{\text{PS}}} + \overbrace{\text{Pe } p_x - \rho \partial_x V}^{\mathcal{F}_{\text{barr}}}, \quad (32)$$

where the phase-separating force  $\mathcal{F}_{\text{PS}}$  gives rise to MIPS, and  $\mathcal{F}_{\text{barr}}$  arises from the barrier. To simplify this expression, we first seek a closed-form expression for the polarisation  $p_x$ . Assuming the (non-conserved) polarisation field relaxes fast compared to  $\rho$ , and also that density gradients are not too large and that the particles have weak alignment, gives rise to (see Appendix D):

$$p_x \approx -\frac{\text{Pe}}{2} \partial_x [\rho d_s(\rho)] - \frac{\text{Pe}}{2} \partial_x \left[ d_s(\rho) \partial_x^2 (\rho d_s(\rho)) + \mathcal{D}(\rho) \partial_x (\rho d_s(\rho)) \partial_x \rho \right]. \quad (33)$$

Physically, the main effect of the third-order gradient terms on the dynamics is to prevent density gradients from growing too large. The same effect can be accomplished in a simpler way by approximating the polarisation as

$$p_x = -\frac{\text{Pe}}{2} \partial_x [\rho d_s(\rho)] + \kappa_0 \partial_x^3 \rho. \quad (34)$$

with constant  $\kappa_0 > 0$ . Substituting this expression into the phase-separating force  $\mathcal{F}_{\text{PS}}$  from (32), and defining  $\kappa = \kappa_0/\text{Pe}$  yields:

$$\mathcal{F}_{\text{PS}} = \partial_x \left[ \ln(1 - \rho) - \frac{\text{Pe}^2}{2} \rho d_s(\rho) \right] + \kappa \partial_x^3 \rho. \quad (35)$$

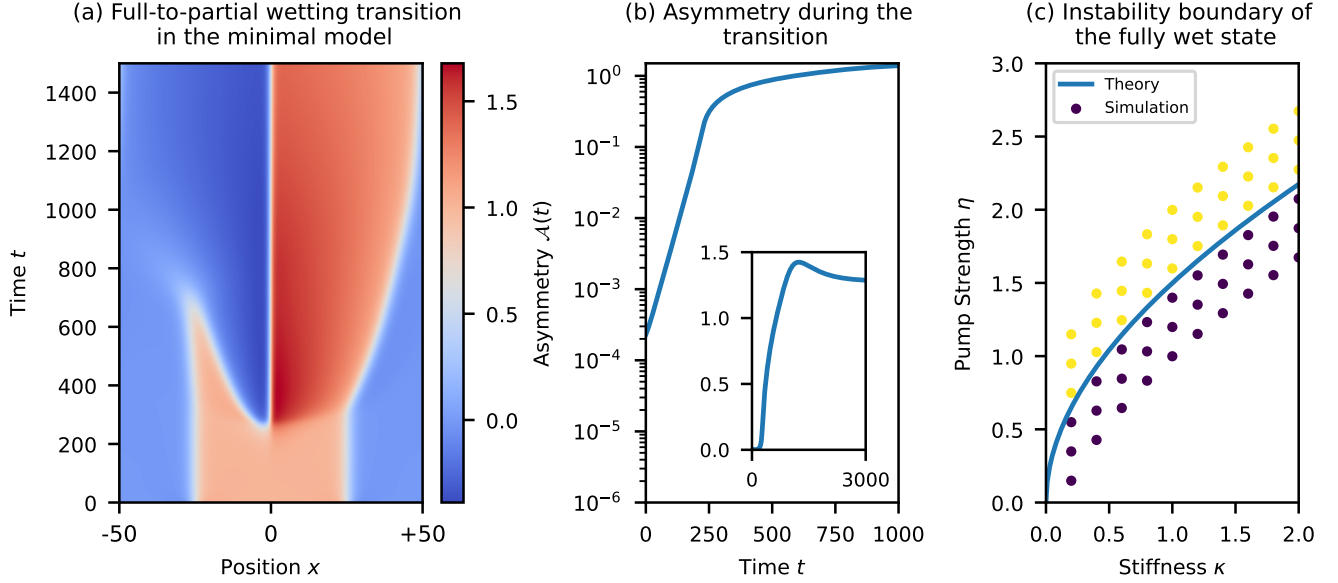


FIG. 7. The minimal model reproduces the instability of the fully-wet state. (a) Example dynamics of a full-to-partial wetting transition; the observed transition resembles the “ratchet-driven instability” seen in the active lattice gas. In particular, the growing linear instability of the fully-wet state, followed by detachment and subsequent evaporation of a liquid droplet from one side, matches the behaviour seen in the full dynamics. The system shown has parameters  $\alpha, \kappa, \bar{\phi} = 1, 1, 0.5$  (b) The asymmetry  $\mathcal{A}$  over time up to  $t = 1000$ , for the dynamics shown in (a). Initial exponential growth (due to the linear instability) is visible from times 0 to 400. (Inset) The same data on a linear scale, showing time up to  $t = 3000$ . (c) Theory vs simulation for the instability boundary of the minimal model, for a range of model parameters. The theoretical instability boundary (plotted for a liquid droplet of size 50) is derived in Appendix D, and is in good agreement with simulation results. All simulations are run with  $L = 100$ .

We recognise  $\mathcal{F}_{\text{PS}}$  as the gradient of a free energy  $F_{\text{PS}}$ :

$$\mathcal{F}_{\text{PS}} = -\partial_x \left( \frac{\delta F_{\text{PS}}}{\delta \rho} \right) \quad (36)$$

$$F_{\text{PS}} = \int_0^{\ell_s} dx \left\{ \frac{\kappa}{2} (\partial_x \rho)^2 + f_\rho(\rho) \right\} \quad (37)$$

where the bulk free energy density is

$$f_\rho(\rho) = \int \frac{\text{Pe}^2}{2} \rho d_s(\rho) - \ln(1 - \rho) d\rho. \quad (38)$$

An explicit expression for  $f_\rho$  can be obtained using (14), and is written in Appendix D. This function becomes a double-welled potential for  $\text{Pe} > \text{Pe}^*$ , giving rise to MIPS.

We now seek a scalar field in one dimension  $\phi(x) : [-\ell_s/2, \ell_s/2] \rightarrow \mathbb{R}$  whose dynamics minimally recreates the behaviour of  $\rho$ , with the same periodic boundary conditions. We simplify the full dynamics by replacing  $f_\rho$  with a simple double-welled potential  $f_\phi = \frac{\alpha}{4} \phi^2 (1 - \phi)^2$ . This simplification replaces the binodals of the full model with constant liquid and vapour densities  $\phi_{l,v} = 1, 0$ , while retaining control over the free-energy barrier between phases. The resulting free energy of the minimal model is then

$$F_{\text{PS}}^\phi = \int_{-\ell_s/2}^{\ell_s/2} dx \left\{ \frac{\kappa}{2} (\partial_x \phi)^2 + \frac{\alpha}{4} \phi^2 (\phi - 1)^2 \right\}. \quad (39)$$

To model the barrier within the minimal model, we only include its ratchet effect. To this end, we replace the potential  $V$  in (18) with a simplified form  $V(x) = \eta \delta(x)$  in  $\mathcal{F}_{\text{barr}}$ , yielding

$$\mathcal{F}_{\text{barr}}(\mathbf{x}) = -\eta \rho(\mathbf{x}) \nabla \delta(x) \quad (40)$$

$$= -\eta \nabla [\rho(\mathbf{x}) \delta(x)] + \eta \nabla \rho \delta(x). \quad (41)$$

The first term of (41) models the effect of volume exclusion from the barrier. This does not contribute to the steady-state current overall as it takes the form of a total derivative, and so its integral over space vanishes. We therefore drop this term and retain only the second term of (41) in the minimal model, identifying this as a pumping (ratchet) effect of the barrier. The resulting force in the minimal model is

$$\mathcal{F}_{\text{pump}}^\phi(x) = \eta (\partial_x \phi) \delta(x). \quad (42)$$

To complete the minimal model, we replace the density-dependent mobility  $\mathcal{M}(\rho)$  of (31) with a constant (taken without loss of generality to be 1). We finally arrive at the following dynamics for the one-dimensional minimal model:

$$\frac{\partial \phi}{\partial t} = -\partial_x J^{(\phi)}(x), \quad (43)$$

where

$$J^{(\phi)}(x) = -\partial_x \left( \frac{\delta F_{\text{PS}}^\phi}{\delta \phi} \right) + \eta \delta(x) \partial_x \phi, \quad (44)$$

and  $F_{\text{PS}}^\phi[\phi]$  is defined in (39). This model replaces MIPS with Cahn-Hilliard phase-separation, while the effect of the barrier is reduced to a local pumping effect at the origin; volume exclusion and all other consequences of the barrier have been removed.

Noting that the first term in the current  $J^{(\phi)}(x)$  is a total derivative, we can integrate over space to find the steady-state density current in this minimal model:

$$J_{\text{ss}}^{(\phi)} = \frac{\eta}{\ell_s} \partial_x \phi(0). \quad (45)$$

Comparing this with the steady-state current of the full dynamics (24) for  $V(x) = \delta(x)$ , which is  $J_{\text{ss}}^{(\rho)} = M[\rho] \partial_x \rho(0)$ , and recalling that  $M[\rho] \sim 1/\ell_s$ , we see that the momentum injection term in the minimal model results in a steady-state current with the same scaling as the full dynamics, in the limit of a large system.

## 2. Wetting states and transitions

The minimal model supports two steady-state solutions, analogous to full and partial wetting (see Appendix D). In the first, a liquid droplet is symmetrically positioned across the pump; in this case, there is no current, and the state corresponds to full wetting. In the second, the liquid bulk is positioned on the edge of the pump, leading to a steady-state current; this corresponds to the partial wetting scenario.

The dynamical transition between these states, presented in Figure 7(a,b), occurs via the same pathway as for the transition in the full dynamics (recall Section IV A and Fig. 6(a, b)). The ratchet first induces symmetry breaking about the barrier through an exponentially growing instability, then a liquid droplet detaches from the barrier and evaporates until the partial wetting steady-state is reached. Although the temporal behaviour of the liquid droplet is different in the minimal model compared to the full case (in particular, it does not “burst”), the same three stages of the transition pathway are observed. Since the minimal model contains only the ratchet effect, and no other consequences of the barrier, we infer that such a ratchet (pumping) effect is alone sufficient to drive the novel transition pathway between wetting states. Although we might expect *any* pumping to lead to instability of the fully-wet state, we only observe the full-to-partial wetting transition above a non-zero critical pumping strength  $\eta^*$  in the minimal model. The ratchet effect is therefore sufficient to also explain why the minimum self-propulsion  $\text{Pe}^*(\epsilon)$ , only above which partial-wetting is observed, is non-zero.

We now present a derivation of the critical pumping strength  $\eta^*$ , in order to prove that it is non-vanishing.

We outline the main steps here, with further details in Appendix D. The instability is controlled by the liquid domain that surrounds the barrier so we consider small perturbations about a homogeneous liquid (see also below):

$$\phi(x, t) = \phi_l + \sum_n \overbrace{A_n \sin(q_n x) + B_n \cos(q_n x)}^{\tilde{\phi}(x)}, \quad (46)$$

for  $q_n = \frac{2\pi n}{L}$  and  $n = 1, 2, \dots$ . The cosine modes do not feel the pumping and so play no role in the instability. At linear order, the mode amplitudes  $A_n$  obey

$$\dot{A}_n = \Gamma_{nm} A_m, \quad (47)$$

where the instability matrix  $\Gamma$  has elements

$$\Gamma_{nm} = - \left( \frac{\alpha}{2} q_n^2 + \kappa q_n^4 \right) \delta_{nm} A_m + \frac{2\eta}{L} q_n q_m. \quad (48)$$

The first term is diagonal in Fourier space and represents stabilising contributions due to effective stiffness ( $\kappa$ ) and bulk free energy density ( $\alpha$ ). The second term, which arises from the ratchet-like driving, introduces non-diagonal mode coupling, it is a rank-1 contribution to  $\Gamma$ . This structure allows for an exact treatment of the largest eigenvalue, using the Sherman-Morrison formula [71]. The onset of the instability occurs at (see Appendix D)

$$\eta_L^* = \frac{\sqrt{2\alpha\kappa}}{\coth(L\sqrt{\frac{\alpha}{8\kappa}}) - \frac{1}{L}\sqrt{\frac{8\kappa}{\alpha}}}, \quad (49)$$

with  $\eta^* = \lim_{L \rightarrow \infty} \eta_L^* = \sqrt{2\alpha\kappa}$  for a large system.

The same analysis reveals that the instability is dominated by large wavelength modes (see Appendix D). Recalling that we are using a homogeneous initial condition as a proxy for the fully-wet state, we can see that this analysis is not necessarily complete; interaction between the pump and the liquid-vapour interfaces (which themselves have a soft translational mode in the fully-wet state) could lead to additional instability, not accounted for above. Nevertheless, numerical results for instability of the fully-wet state show very good agreement with (49), see Figure 7(c). This indicates that the density fluctuations within the liquid domain are dominant in driving the instability, consistent with our analysis.

In summary, our analysis of the dynamical transitions has revealed a novel pathway from full-to-partial wetting, which would be inaccessible for passive fluids. We have understood the origin of this pathway through a minimal model, wherein the consequences of the activity and the barrier are reduced to only the pumping effect. This minimal model is able to recreate the observed novel transition pathway, with instability only emerging at a finite, calculated, pumping strength – we infer that the ratchet effect on the barrier is the key ingredient that drives the novel transition pathway.

## V. DISCUSSION

### A. Summary of results

We have studied active wetting by considering the hydrodynamic behaviour of an active lattice gas in the presence of a smooth permeable barrier, under periodic boundary conditions. This geometry is analogous to a slit geometry widely used to study equilibrium wetting [64]. We take as control parameters the barrier height  $\epsilon$  and self-propulsion  $Pe$ .

The surface phase diagram reveals wetting states whose density profiles are analogous to the equilibrium wetting states of dry, partially-wet, and fully-wet. As our model is hydrodynamic and (in consequence) large-scale, we conclude that these states are true macroscopic wetting states, instead of microscopic accumulations of active matter. This observation is supported by particle studies in which wetting-like states have been observed [30–32, 36, 39, 55]. Our work avoids the challenges associated with finite-size scaling in such simulations, justifying our conclusion that wetting is a macroscopic effect.

We found a drying transition at  $\epsilon = 0$ , and a wetting transition at finite  $\epsilon = \epsilon^*(Pe)$ . We investigated the wetting transition in further detail, observing a diverging film width on the dry side, vanishing hysteresis, the onset of linear instability, and a pitchfork bifurcation in the asymmetry order parameter  $\mathcal{A}$ . These are the salient characteristics of critical wetting in passive fluids [41–43], and so we conclude that the nonequilibrium transition between full- and partial-wetting states is critical. This finding is supported by previous particle-based simulations, which have shown that active wetting appears critical in two dimensions [30, 32].

We have demonstrated that asymmetric density profiles around symmetric permeable barriers lead to a ratchet effect. This results in a steady-state circulating current in the partially-wet state, which is suppressed as  $J_{ss}^{(\rho)} \sim \ell_s^{-1}$  in large systems. Although the observation of a ratchet effect in this context is novel, ratchets have previously been recognised as a general consequence of asymmetric barriers in active matter [21–23, 27, 28]. Additionally, steady-state currents have already been understood as a key characteristic of partial wetting states in active matter [55].

We have observed and characterised a novel dynamical transition pathway from full- to partial-wetting in the active system; this involves the detachment, and subsequent evaporation, of a liquid droplet from the barrier. Due to the creation of additional interfaces, this pathway is energetically inaccessible in passive fluids, and so we conclude that this is an inherently nonequilibrium pathway. We further analysed this active pathway by deriving a minimal model for the hydrodynamic system, in which the consequences of activity are reduced to passive phase separation and a local ratchet effect. We demonstrated that the wetting transition in this minimal model proceeds via the same dynamical pathway, and occurs only

above a non-zero critical pumping strength  $\eta^*$ . We used a linear stability analysis to calculate an analytical expression for  $\eta^*$ . An important conclusion of this additional calculation is that the pumping effect is alone sufficient to drive the novel full-to-partial transition pathway, while fully-wet states remain stable at low pumping strengths.

To conclude, we have robustly demonstrated the existence of macroscopic active wetting states, and characterised the surface phase diagram. We have shown that these states behave remarkably similarly to their passive counterparts, including a critical wetting transition. Our hydrodynamic framework therefore establishes a direct connection between the equilibrium theory of wetting [42], and active wetting phenomenology. Moreover, we have shown that activity results in a pumping effect on a permeable barrier. We have understood two consequences of this effect, namely a steady-state current in the partially-wet state and a novel full-to-partial transition pathway. Our hydrodynamic framework therefore allows us to clearly identify the correspondences between passive and active wetting, while characterising their differences and understanding the origins of these differences.

### B. Outlook

There are several promising directions for future work which build on the results presented in this paper. One obvious extension would be to reintroduce density-dependence in the direction(s) parallel to the wall, which would allow investigation of the “droplet” geometry of equilibrium wetting, facilitating measurement of contact angles and interfacial profiles. (Additionally, the presence of several droplets on both sides of the barrier in the partial wetting state could result in a circulating flux pattern on the macroscopic scale, even with closed boundary conditions.) Such a description would therefore help connect this work to other investigations of equilibrium [41, 65] and active [37–39, 55] wetting.

Another extension would be to introduce dynamical noise to the system, which can be done in our lattice-based approach in a controlled manner via a leading-order correction to the hydrodynamic equations [61]. The inclusion of dynamical noise and fluctuations can have dramatic consequences in equilibrium [64] and non-equilibrium [30] wetting phenomenology, including changing the stability of steady-states and the order of transitions. Investigating the consequences of noise could therefore allow us to confirm the generality and robustness of the findings presented in this work.

Finally, it is important to consider how the effects presented here might be observed or harnessed experimentally. A promising experimental direction could be to recreate active wetting in a slit geometry using light-activated colloidal particles [26, 72, 73], in which activity can be spatially confined to the central region of a slit

without the need for confinement in the perpendicular direction. This approach (which allows for quasi-one-dimensional periodic boundary conditions, for example by global confinement in a toroidal region [26]) may enable direct measurement of asymmetries, currents, and wetting states, and could provide direct experimental evidence of the ratchet effects described here.

## ACKNOWLEDGMENTS

We thank Bob Evans, Francesco Turci, and Maria Bruna for insightful discussions and valuable feedback throughout this work. This work was supported by the Engineering and Physical Sciences Research Council grant number EP/W524633/1.

## APPENDIX A: EQUILIBRIUM THEORY OF CRITICAL WETTING

### 1. Cahn theory of wetting

We briefly review some of the results of the Cahn theory of wetting, as discussed in [41, 42]. These are useful points of comparison with the active wetting model, and are stated in the main text. Minimisation of the free energy (3) results in a condition on the fluid density at the wall  $\rho_s \equiv \rho(0)$ :

$$-\frac{df_w}{d\rho_s} = \sqrt{2\kappa W(\rho_s)}. \quad (\text{A1})$$

where, without loss of generality, we have assumed that the bulk free-energy density  $W(\rho)$  has minima  $W(\rho_l) = W(\rho_v) = 0$ . This may give one or multiple solutions for the surface density  $\rho_s$ ; stable solutions are shown by the black points in Figure 8. If the solution  $\rho_s \in (\rho_v, \rho_l)$ , the density profile may go to  $\rho_v$  as  $x \rightarrow \infty$  (in the bulk) to form a partially-wet/dry wall, or increase to  $\rho_l$  to form a fully-wet wall. If  $\rho_s \geq \rho_l$ , decay to the liquid density in the bulk is always energetically favourable, and the wall is always fully wet.

In a first-order wetting transition, two stable solutions exist for  $\rho_s$ , with  $\rho_1 \in (\rho_v, \rho_l)$  and  $\rho_2 > \rho_l$ . The first solution  $\rho_1$  therefore corresponds to partial wetting, and the second solution  $\rho_2$  to full wetting (see Figure 8(a)). The transition between these is determined by a Maxwell construction [41]. The surface density changes discontinuously, and metastable solutions for  $\rho_s$  exist.

Second-order (critical) wetting occurs when there is only one solution for  $\rho_s$  near the wetting transition, i.e. if  $c_2 > \lim_{\rho \rightarrow \rho_l} \frac{\partial}{\partial \rho} [\sqrt{2\kappa W(\rho)}]$ . In this case,  $\rho_s$  passes continuously through  $\rho_l$  and no metastable states exist.

Just below a critical wetting transition, we have  $\rho_s = \rho_l - \delta$ . By minimising the free energy of the density profile away from the wall, we find  $\delta \propto e^{-\zeta/\xi}$ , where  $\zeta$  is the thickness of the wetting film and  $\xi$  is the liquid-vapour

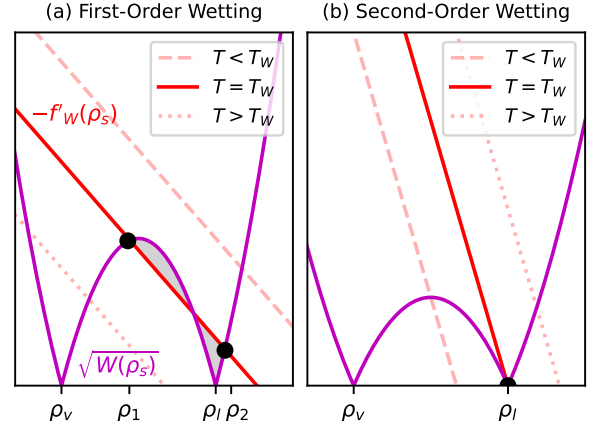


FIG. 8. Illustration of First- and Second-Order wetting in the Cahn theory. (a) In a first-order wetting transition,  $c_2$  is small, and multiple solutions for  $\rho_s$  exist; the discontinuous transition between the solutions is determined by a Maxwell condition. (b) In a second-order transition, only one solution exists for  $\rho_s$ , and the wetting transition occurs when this passes continuously through  $\rho_l$ .

interfacial width. Taking temperature as a control parameter, the free energy of this film is then given by (for a detailed discussion, see [41]):

$$F_{\text{film}}(\zeta) = F_0 - \alpha(T)e^{-\zeta/\xi} + \beta(T)e^{-2\zeta/\xi}, \quad (\text{A2})$$

where  $\alpha \propto (T_w - T) + \mathcal{O}((T_w - T)^2)$ , and  $\beta = \text{constant} + \mathcal{O}(T_w - T)$ . The effect of temperature  $T$  is to control the shape of  $W(\rho)$ ; at a higher temperature, the coexistence densities become closer and the energetic barrier between these densities becomes smaller. The optimal width of the liquid film  $\zeta^*$ , which minimises the free energy (A2), is thus given by:

$$\zeta^* = -\xi \log(T_w - T) + \text{const.} \quad (\text{A3})$$

The width of a liquid film near a critical-wetting transition is therefore diverges logarithmically. In contrast, the film width at a first-order wetting transition will jump discontinuously from microscopic ( $\sim \xi$ ) to macroscopic. A similar analysis demonstrates that the divergence of the liquid film width is logarithmic approaching a critical transition for any other control parameter (such as the wall attractiveness  $c_1$ , as in the main text).

In a slit geometry, it is favourable for 2 initially equal liquid films of with  $\zeta_0$  to remain equal in size (i.e. the system will remain fully wet) iff:

$$\left. \frac{d^2 f}{d\zeta^2} \right|_{\zeta_0} \leq 0, \quad (\text{A4})$$

which, for  $\zeta_0 \rightarrow \infty$ , occurs exactly when  $T \geq T_w$ . Below this critical temperature, it is favourable for mass to redistribute from one film to another (via a translational instability) until one film is microscopic ( $\sim \xi$ ) and

the other is macroscopic; this is the partial wetting scenario. A fully-wet state is therefore unstable below this critical transition temperature in a slit geometry, and a partially-wet state is unstable above it. Thus, there are no metastable states in the critical wetting scenario, as expected. Once again, this analysis is general for any other choice of order parameter.

## 2. Asymmetry order parameter

We now find the behaviour of the asymmetry order parameter just below the critical wetting transition. Consider wetting in a slit geometry of total width  $L_{\text{tot}} > 2L$ , with 2 liquid films of thickness  $L - \delta, L + \delta$  on either wall (and without loss of generality  $\epsilon \in [0, L]$ ). We assume that  $L \gg \xi$ , such that the liquid-vapour interfaces are well-resolved. The free energy due to the wetting layers becomes:

$$F_{\text{film}}(\delta) = 2\alpha(T)e^{-L/\xi} \cosh(\delta/\xi) + 2\beta(T)e^{-2L/\xi} \cosh(2\delta/\xi). \quad (\text{A5})$$

To find the optimal  $\delta$ , we set  $\frac{\partial F_{\text{film}}}{\partial \delta} = 0$ , yielding the condition:

$$\cosh(\delta/\xi) = \frac{\alpha}{4\beta} e^{L/\xi}. \quad (\text{A6})$$

As the liquid film varies continuously approaching a critical wetting transition, we expect  $\delta$  to be small just below criticality. So expanding  $\cosh(\delta/\xi) \simeq 1 + \frac{1}{2}(\frac{\delta}{\xi})^2$ :

$$\delta + \mathcal{O}(\delta^2) = \xi \sqrt{\frac{\alpha}{2\beta} e^{L/\xi} - 2}. \quad (\text{A7})$$

The asymmetry parameter can be expressed as  $\mathcal{A} = \frac{L^+ - L^-}{L^+ + L^-} = \frac{\delta}{L} \in [0, 1]$  (this equivalent to (7)). Define  $\bar{\alpha} = \alpha - 2\beta e^{-L/\xi}$ . We may assume that this is proportional to a modified critical temperature near criticality, i.e.  $\bar{\alpha} = \kappa(\bar{T}_w - T) + \mathcal{O}(|\bar{T}_w - T|^2)$ . The modified critical temperature accounts for a finite system size correction:  $\bar{T}_w = T_w + \mathcal{O}(e^{-L/\xi})$ . With these definitions, we have the following behaviour for  $\mathcal{A}$  near a critical wetting transition, in a finite system:

$$\mathcal{A} = \begin{cases} 0 & T \geq \bar{T}_w, \\ \left[ \frac{\xi}{L} \sqrt{\frac{\kappa}{2\beta}} e^{\frac{L}{2\xi}} \right] (\bar{T}_w - T)^{1/2} & T < \bar{T}_w. \end{cases} \quad (\text{A8})$$

One sees that this asymmetry exhibits a pitchfork bifurcation near a critical wetting transition, with characteristic exponent 1/2. In the large-system limit  $L \rightarrow \infty$  then  $\mathcal{A} \rightarrow 1$  for all  $T < T_w$ ; this effect is signalled in Eq. (A8) by the divergence of the prefactor in this limit. In practice, this means that observation of power-law scaling in Eq. (A8) requires relatively small system sizes ( $L/\xi \sim 1$ ), and  $T$  close to  $\bar{T}_w$ .

## APPENDIX B: DYNAMICS IN THE PRESENCE OF AN EXTERNAL POTENTIAL

### 1. Derivation from free energy

As discussed in the main text, the hydrodynamic equation (11) was derived previously [60] for the special case of uniform potential. We show here how the effect of a spatially varying potential  $V(\mathbf{x})$  can be added. For  $V = 0$ , Eq. (11) can be factorised [60] as

$$\partial_t f = \nabla \cdot \int \sigma_f(\mathbf{x}, \theta, \theta') \left[ D_E \nabla \frac{\delta S}{\delta f(\mathbf{x}, \theta')} + v_0 \mathbf{e}_{\theta'} \right] d\theta' + D_O \partial_\theta \left[ f(\mathbf{x}, \theta) \partial_\theta \frac{\delta S}{\delta f(\mathbf{x}, \theta)} \right], \quad (\text{B1})$$

where the free energy is

$$S[f] = \int d\mathbf{x} [1 - \rho(\mathbf{x})] \log[1 - \rho(\mathbf{x})] + \int d\mathbf{x} d\theta f(\mathbf{x}, \theta) \log(2\pi f(\mathbf{x}, \theta)) \quad (\text{B2})$$

and

$$\sigma_f(\mathbf{x}, \theta, \theta') \equiv s(\rho(\mathbf{x})) f(\mathbf{x}, \theta) f(\mathbf{x}, \theta') + d_s(\rho(\mathbf{x})) f(\mathbf{x}, \theta) \delta(\theta - \theta') \quad (\text{B3})$$

plays the role of a mobility; we have used the shorthand  $s(\rho) = \frac{1 - d_s(\rho) - \rho}{\rho} = \mathcal{D}(\rho) - 1$ . This formulation of the equation of motion allows the terms involving  $\delta S / \delta f$  to be identified with equilibrium-like processes, which act to minimise  $S$ . By contrast, the term proportional to  $v_0$  is the non-equilibrium self-propulsion force.

The potential  $V$  is added as an extra equilibrium-like force: one adds an additional term to the free energy by replacing  $S[f] \rightarrow S[f] + \int d\mathbf{x} \rho(\mathbf{x}) V(\mathbf{x})$ . Substituting into (B1) then leads to (11). Note that adding the potential results in  $\frac{\delta S}{\delta f(\mathbf{x}, \theta')} \rightarrow \frac{\delta S}{\delta f(\mathbf{x}, \theta')} + V(\mathbf{x})$ ; the additional term is independent of  $\theta'$ , which reflects that the force from the barrier does not depend on the particle orientation. Noting also that  $\int \sigma_f(\rho, \theta, \theta') d\theta' = f(\theta)$  explains why  $V$  appears in such a simple way in Eq. (11).

### 2. Steady-state current

We derive (24) for the steady state density current. For completeness, we work with the dimensional dynamics (11), although the results quoted in the main text correspond to the dimensionless system (16). We start from the expression for the spatial probability current in (12, 13), writing only the  $x$ -component as this is the only direction in which the current is non-vanishing:

$$J_x(x, \theta) = -D_E [d_s(\rho) \partial_x f + f \mathcal{D}(\rho) \partial_x \rho + (1 - \rho) f \partial_x V] + v_0 [f s(\rho) p_x + \cos(\theta) f d_s(\rho)] \quad (\text{B4})$$

Integrating over  $\theta$  and making use of the definitions of  $s(\rho), \mathcal{D}(\rho)$ , we obtain the spatial density current

$$J^{(\rho)} = -D_E [\partial_x \rho + (1 - \rho) \rho \partial_x V] + v_0 (1 - \rho) p_x. \quad (\text{B5})$$

In steady state, the density current must be divergence-free, and so with one non-trivial spatial dimension this must be a constant  $J^{(\rho)}(x) = J_{\text{ss}}^{(\rho)}$ . Dividing (B5) through by  $1 - \rho$ , integrating over space with periodic boundaries, and using the identity  $\int_0^L \mathbf{p} \, dx = 0$  in steady-state (proven below), yields:

$$J_{\text{ss}}^{(\rho)} = M[\rho] \int_0^L V(x) \partial_x \rho \, dx. \quad (\text{B6})$$

where  $M[\rho] = D_E / \int_0^L \frac{1}{(1-\rho)} dx$  as in (25). Integration by parts on (B6) yields (24), written in dimensionless units.

The above result used  $\int_0^L \mathbf{p} \, dx = \mathbf{0}$  in steady-state, which we now derive. (This relies on the fact that particle orientations diffuse independently so the one-particle distribution of orientations is uniform in steady state.) We work on the equation of motion for  $\mathbf{p}$ :

$$\begin{aligned} \partial_t \mathbf{p} &= \partial_t \int f(x, \theta, t) \mathbf{e}_\theta \, d\theta \\ &= \int \{ -D_E \nabla \cdot \mathbf{J}_{\text{diff}} - v_0 \nabla \cdot \mathbf{J}_{\text{activity}} + D_O \partial_\theta^2 f \} \mathbf{e}_\theta \, d\theta. \end{aligned} \quad (\text{B7})$$

Taking the spatial integral of this equation, we note that the first two terms on right hand side are pure divergences so they vanish. Then integrate by parts twice in the final term before using again the definition of  $\mathbf{p}$ . We obtain

$$\partial_t \int_0^L \mathbf{p}(\mathbf{x}) \, d\mathbf{x} = -D_O \int_0^L \mathbf{p}(\mathbf{x}) \, d\mathbf{x}, \quad (\text{B8})$$

to which the only steady-state solution is  $\int_0^L \mathbf{p}(\mathbf{x}) \, d\mathbf{x} = 0$ , as required.

## APPENDIX C: DETAILS OF THE NUMERICAL METHOD

A Python implementation of the numerical methods discussed below, as well as the code used to generate figures in this work, is available at [74].

### 1. Timestepping routine for full PDEs

To carry out simulations of the system, we use an explicit time-stepping routine. We first rewrite the dynamics in the form:

$$\partial_t f = -\partial_x [M^x U^x] - \partial_\theta [M^\theta U^\theta], \quad (\text{C1})$$

where  $M^x, M^\theta$  are the scalar mobilities and  $U^x, U^\theta$  are the velocity fields. The mobilities are given by  $M^x = f d_s(\rho)$ ,  $M^\theta = f$ , and the velocity fields by:

$$\begin{aligned} U^x &= -D_E \left[ \partial_x (\log f) + \frac{\mathcal{D}(\rho)}{d_s(\rho)} \partial_x \rho + \frac{(1 - \rho)}{d_s(\rho)} \partial_x V \right] \\ &\quad + v_0 \left[ \cos(\theta) + \frac{ps(\rho)}{d_s(\rho)} \right] \end{aligned} \quad (\text{C2})$$

and

$$U^\theta = -D_O \partial_\theta [\log f]. \quad (\text{C3})$$

We then follow the same first-order update scheme as Section 4 of [60] and Appendix E of [63], but modified with these slightly different angular and spatial dynamics. We discretise the system into an  $N_x \times N_\theta$  grid, and use an upwind condition to calculate the fluxes, updating the discretised field  $f_{ijk}$  accordingly. Finally, we use a CFL condition for an adaptive timestep<sup>5</sup> (as in [60, 63]):

$$\Delta t_{\text{max}} = \min \left( \frac{\Delta x}{a \max |U^x|}, \frac{\Delta \theta}{b \max |U^\theta|}, \tau_{\text{max}} \right). \quad (\text{C4})$$

We find that parameters  $a = b = 6$ ,  $\tau_{\text{max}} = 10^{-4}$  are sufficient to ensure numerical stability and accuracy, while remaining practical to compute. We typically ran simulations with  $N_x = 200$  and  $N_\theta = 30$ , although we verified that results are accurate when compared with finer grids. We always use an even  $N_\theta$  to ensure the simulation is parity-symmetric.

Various checks were performed to verify that this PDE scheme functions as expected; for example, the mean density is conserved up to a computational error that is typically of order  $10^{-10}$ , the averages of higher angular moments vanish similarly in steady-state, and the stability boundary matches the theoretical prediction of [60] (see below). Symmetry-breaking events were confirmed to be random in direction, as expected – for example, in a trial of 70 partially-wet states, the liquid layer formed on the left of the barrier in 37 simulations. The dynamics of full wetting was qualitatively compared to the particle-level simulations of [36] and [30], confirming that the hydrodynamic equations reproduce the appropriate physical behaviour.

### 2. Generation of binodal and spinodal

#### a. Theoretical and numerical instability boundary

To generate a theoretical bound for the onset of instability, we follow the method outlined in Section 3 of [60].

<sup>5</sup> Although the CFL condition is necessary to prevent instabilities/inaccuracy arising from advective behaviour, it does not address issues related to the density leaving its valid range of  $\rho \in [0, 1]$ . For this reason,  $a, b > 1$  and finite  $\tau_{\text{max}}$  are necessary to ensure stability.

As the spinodal is defined in the absence of a potential, our modified equations have no effect on the linear stability analysis. For the theoretical spinodal line shown in Figure 2, we truncate the (infinite) instability matrix of a homogeneous state to a  $10 \times 10$  matrix, which is sufficient for good convergence as discussed in [60].

To generate the numerical spinodal, we follow the same method as in [60]. We initialise the system with a homogeneous density field, and then add a small perturbation corresponding to the eigenfunction with the largest instability. We then classify the phases according to the mean square deviation of the density field from the homogeneous state, using the same classification as in [60]. Although the spinodal is formally defined in the limit of large system size, our simulations are run in a system size of  $L_x = 20$  with a grid of  $200 \times 30$  points. We find good agreement between theory and numerics, as shown in Figure 2. No significant deviations are visible if a larger system size or smaller lattice spacing are used. This provides a check for the validity of our numerical routine and computational parameters, as we can see that the physics of stability are preserved appropriately.

### b. Numerical binodal

A theoretical expression for the binodal is not available, so we must rely on numerical methods to generate it. We use the following routine:

1. Initialise a simulation from a homogeneous state plus a maximal instability perturbation as above. The parameters used are:  $L = 20, N_x = 400, N_\theta = 30, \rho = \rho^* = 0.6585$ , and  $v_0$  is a specified parameter. If  $v_0 > 15$ , we instead use  $N_x = 800$  so the (sharper) interfaces remain well-resolved.
2. Evolve this system to time  $t_0 = 200$ , after which a single liquid droplet has formed.
3. Initialise a new simulation with the same parameters apart from  $L$ , but using reflecting boundary conditions (i.e.  $\left. \frac{df(x, \theta)}{dx} \right|_{x=0, L} = 0$ ), in a system of size  $L = 40$ . Take one half of the previous simulation as a new initial condition, such that the profile contains vapour on one side and liquid on the other, with a single interface.
4. Evolve to a time  $t_1 = 200$ . Identify the liquid and vapour densities as the maximum and minimum densities in this final state.
5. Repeat for 8 uniformly spaced values of  $v_0 \in (v_{0, \text{crit}}, 6.0]$  and another 10 values in the range  $v_0 \in (6.0, 30.0]$ .

The numerical binodal is then generated by interpolating between these data-points. The effective size over

which the interface is resolved is  $L = 40$ , and so we expect convergence to the bulk values given a typical interfacial scale  $l_D = 1.0$ . Simulations were run for isolated points on the binodal with a larger system size and finer grid spacing; no significant departure was seen from the interpolated binodal, and so we assume that the above parameters are sufficient for good convergence. For example, the binodals for  $v_0 = 10.0$  were estimated at  $(\rho_v, \rho_l) = (0.1086, 0.9855)$  and  $(\rho_v, \rho_l) = (0.1115, 0.9872)$  for systems of size  $L = 40, L = 50$  respectively, a difference of about 0.2%. similar checks were performed for across the binodal, and all quoted values did not change by more than 1% when the system size was increased to  $L = 50$ . Therefore, we are confident that the binodal is sufficiently converged for the purposes of the illustrative figure.

### 3. Classifying wetting states

In simulations run for a sufficiently long time, we observe that the system always reaches one of the four wetting states described. However, many of the runs have not yet reached steady-state at  $t = t_f$ , so we must classify the state according to the history of the run as well as the final state. This allows us to determine which state the system will arrive at after a long time, using the procedure outlined below. Isolated tests of the below procedure were performed, and it is generally accurate; errors only appear in classification very close to the transition lines (usually at a distance less than the resolution of the surface phase diagram).

For the non-varied parameters, we choose model parameters  $(D_E, D_O, \bar{\rho}, L, d) = (1, 1, \bar{\rho}_{\text{crit}}, 12, 0.5)$  and computational parameters  $N_x = 500, N_\theta = 20, \Delta t_{\text{max}} = 10^{-5}$ . Repeating the analysis at single points with a finer grid spacing or shorter  $\Delta t$  does not lead to any significant difference in temporal behaviour or spatial structure. Our choices ensure that  $L \gg l_d, d \gg \Delta x$ , i.e. the system is much larger than the typical scale of phase interfaces or the barrier, both of which are well resolved on the grid.

States are classified first according to whether they are phase separated at  $t_f = 200$ , then by whether they are pinned, and then the partial/full wetting cases are resolved. Finally the full-to-partial wetting line is calculated. This we now describe.

*a. Phase separated vs homogeneous states.* The scale of fluctuations outside of the barrier is measured using the variance of density fluctuations away from the barrier:

$$\sigma_\rho^2 = \int_0^{L/2-d} (\rho(x) - \bar{\rho})^2 dx + \int_{L/2+d}^L (\rho(x) - \bar{\rho})^2 dx. \quad (\text{C5})$$

We exclude the space  $x \in [L/2 - d, L/2 + d]$  in order to remove the effect of volume exclusion on the barrier. States are classified as homogeneous if  $\sigma_\rho^2 < 0.01$ . The

orange phase-separation line shown in Figure 3(a) is a smooth line fit to the data and of form  $\text{Pe}_{\text{PS}} = \frac{a}{b+c\epsilon} + d$ .

*b. Unpinned/dry vs wet states.* As a barrier does not exist for  $\epsilon = 0$ , all states with  $\epsilon = 0$  are trivially dry/unpinned. To find whether the states at finite  $\epsilon$  are pinned to the barrier, their density profiles are examined. If the barrier is within  $l_D$  of a liquid-vapour interface or inside the liquid bulk, we consider the state to be wet. With this definition, all solutions at finite  $\epsilon$  are classified as wet in steady-state. Experiments at smaller  $\epsilon$  than the minimum value reported remain wet, indicating that any finite barrier height leads to wetting.

*c. Partially-wet vs fully-wet states.* Finally we settle the distinction between partially- and fully-wet: states are classified as fully-wet if  $\mathcal{A} < 10^{-3}$  (i.e. the wetting films are approximately the same width); otherwise, they are classified as partially-wet.

*d. Full-to-partial wetting transition.* In order to generate the wetting line shown in Fig. 3(a), we make use of the linear instability of the fully-wet state. We measure the value of  $\dot{\mathcal{A}}/\mathcal{A}$  at the time such that  $\mathcal{A} = 10^{-3}$ . A linear equation is then fit to these data-points of form  $\dot{\mathcal{A}}/\mathcal{A} = a(\epsilon - \epsilon^*(\text{Pe}))$ , using the 3 smallest values of  $\dot{\mathcal{A}}/\mathcal{A}$  at a given  $\text{Pe}$  (3 values are taken in order to ensure the fit is within the linear instability regime). This gives an estimate for  $\epsilon^*(\text{Pe})$ , shown with the blue wetting line in 3(a). The advantage of this method, compared to directly measuring the asymmetries and allocating states accordingly, is that we do not need to wait an exponentially long time for states near the transition to reach the partially-wet state. This therefore allows an accurate calculation of the wetting line with a reasonable computational cost. Only a small discrepancy is observed between the wetting line and the classification of states, as expected.

## APPENDIX D: MINIMAL MODEL

We present detailed calculations for the minimal model described in Sec. IV B.

### 1. From active lattice gas to minimal model

We motivate the minimal model (43) as an approximation to the dynamics of the active lattice gas. We work here in arbitrary dimensions, although results are quoted in the main text in one spatial dimension, to match the desired dimensions of the minimal model. We start by writing the explicit dynamics of  $\mathbf{p}(x, t)$ , by performing the integral over  $\theta$  on the right hand side of (B7), to yield

$$\begin{aligned} \partial_t p_i &= D_E \nabla \cdot [d_s(\rho) \nabla p_i + \mathcal{D}(\rho) p_i \nabla \rho + (1 - \rho) p_i \nabla V] \\ &- v_0 \nabla \cdot [s(\rho) p_i \mathbf{p}] + \sum_j \partial_j \left[ \frac{d_s(\rho)}{2} Q_{ij} \right] + \partial_i \left[ \frac{d_s(\rho)}{2} \rho \right] - D_O p_i, \end{aligned} \quad (\text{D1})$$

where the traceless nematic alignment tensor is defined  $Q_{ij}(\mathbf{x}, t) = 2 \int f(\mathbf{x}, \theta, t) (\mathbf{e}_\theta)_i (\mathbf{e}_\theta)_j d\theta - \rho(\mathbf{x}, t) \delta_{ij}$ .

We focus on regions away from the barrier. We seek an effective theory for the density alone. To this end, we make three approximations: (i) the polarisation  $\mathbf{p}$  relaxes faster than the density  $\rho$  allowing an adiabatic elimination; (ii) density gradients are not too large, which enables gradient expansion; (iii) particles' alignment is weak, which means  $|\mathbf{p}|^2 \ll 1$  and  $\underline{Q} \approx 0$ . This last approximation is natural, given the previous two.

Moving to dimensionless units as in (16) and considering regions away from the barrier we use weak alignment, and adiabatic elimination of the “fast” field  $\mathbf{p}$ , to obtain:

$$p_i = \nabla \cdot [d_s(\rho) \nabla p_i + \mathcal{D}(\rho) p_i \nabla \rho] - \frac{\text{Pe}}{2} \partial_i [\rho d_s(\rho)]. \quad (\text{D2})$$

Plugging (D2) into itself recursively, and retaining only terms up to third-order in the gradient, yields

$$\begin{aligned} p_i &= -\frac{\text{Pe}}{2} \nabla \cdot \left[ d_s(\rho) \partial_i \nabla (\rho d_s(\rho)) \right. \\ &\quad \left. + \mathcal{D}(\rho) \partial_i (\rho d_s(\rho)) \nabla \rho \right] - \frac{\text{Pe}}{2} \partial_i [\rho d_s(\rho)]. \end{aligned} \quad (\text{D3})$$

Physically, the main effect of the first term (which is third order in gradients) on the dynamics is to prevent density gradients from growing too large. In constructing the minimal model, we reproduce this same effect in a simpler way by approximating the polarisation as

$$p_i \approx -\frac{\text{Pe}}{2} \partial_i [\rho d_s(\rho)] + \kappa_0 \partial_i (\nabla^2 \rho) \quad (\text{D4})$$

with constant  $\kappa_0 > 0$ .

The bulk force that drives phase separation, given in (32), is

$$\mathcal{F}_{\text{PS}} = \nabla \ln(1 - \rho(x)) + \text{Pe} \mathbf{p}. \quad (\text{D5})$$

Using (D4), and defining  $\kappa = \kappa_0/\text{Pe}$ , we can rewrite this force as a total derivative:

$$\mathcal{F}_{\text{PS}} = \nabla \left[ \ln(1 - \rho) - \frac{\text{Pe}^2}{2} \rho d_s(\rho) + \kappa \nabla^2 \rho \right]. \quad (\text{D6})$$

To simplify this model further, we first consider the terms with only one gradient. Recalling that for Cahn-Hilliard dynamics,  $\mathcal{F}_{\text{PS}} = -\nabla(\delta F_{\text{PS}}/\delta \rho)$ , we identify the bulk free energy  $F_{\text{PS}}$  and bulk free energy density  $f_{\text{PS}}$ :

$$\begin{aligned} F_{\text{PS}}[\rho] &= \int \frac{\kappa}{2} |\nabla \rho|^2 + f_{\text{PS}}(\rho) d\mathbf{x}, \\ f_{\text{PS}}(\rho) &= (1 - \rho) \ln(1 - \rho) + c + \mu \rho + \frac{\text{Pe}^2}{2} \int \rho d_s(\rho) d\rho. \end{aligned} \quad (\text{D7})$$

where  $\mu, c$  are arbitrary constants which do not affect the dynamics. Using the polynomial approximation for  $d_s(\rho)$

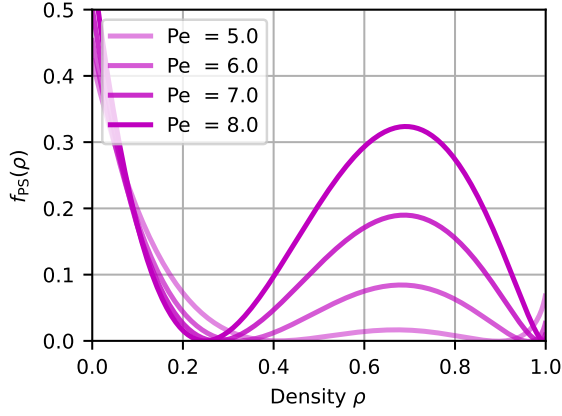


FIG. 9. The bulk free energy density  $f_{\text{PS}}(\rho; \mu, c)$ , for various  $\text{Pe} > \text{Pe}^*$ . The arbitrary parameters  $\mu, c$  have been chosen such that the free energy minima are both at 0.

given in (14), an explicit expression for the final term of (D7) can be obtained:

$$\int \rho d_s(\rho) d\rho = \frac{\alpha(2\alpha-1)}{5(2\alpha+1)}\rho^5 - \frac{\alpha^2}{2\alpha+1}\rho^4 + \frac{\alpha+1}{3}\rho^3 - \frac{1}{2}\rho^2, \quad (\text{D8})$$

where  $\alpha = \pi/2 - 1$ . For sufficiently large  $\text{Pe}$ , the bulk free energy  $f_{\text{PS}}$  becomes a non-convex function of  $\rho$ , giving rise to phase separation. Using the above expression for  $\mathcal{D}$ , this critical activity can be numerically obtained, yielding  $\text{Pe}^* \simeq 4.3$ , in approximate agreement with value obtained by linear stability analysis (see Section C 2). The bulk free energy density is shown for a range of  $\text{Pe}$  values above the critical activity in Figure 9.

## 2. Steady states of the minimal model

We demonstrate the existence of full and partial wetting solutions in the minimal model. These are steady-state 1d solutions to (43), which obey

$$0 = -\frac{\partial}{\partial x} \left[ \overbrace{\frac{\alpha}{2}(6\phi^2 - 6\phi + 1)\partial_x\phi + \kappa\partial_x^3\phi}^{\text{CH Free Energy Minimisation}} + \overbrace{\eta\partial_x\phi\delta(x)}^{\text{Pump}} \right]. \quad (\text{D9})$$

The full wetting phase is a minimum of the Cahn-Hilliard free energy that obeys  $\phi(x) = \phi(-x)$  and  $\phi(0) \approx 1$ . For average densities inside the binodal, this solution has two domain walls arranged symmetrically on either side of the origin. The Cahn-Hilliard force vanishes everywhere for this state; since the solution is even, i.e.  $\partial_x\phi(0) = 0$ , then the pumping force also vanishes and this fully-wet state solves (43). The effect of the pump on the *stability* of this solution is discussed in the next section.

For the partially-wet steady-state we set the current in

(44) be a constant

$$J_{\text{ss}}^{(\phi)} = \frac{\alpha}{2}(6\phi^2 - 6\phi + 1)\partial_x\phi + \kappa\partial_x^3\phi + \eta\partial_x\phi\delta(x), \quad (\text{D10})$$

Integrating again across  $x = 0$  we have that  $\phi, \partial_x\phi$  must be continuous and we obtain a jump condition on the second derivative of  $\phi$ :

$$\frac{\partial^2\phi}{\partial x^2}\Big|_{0+} - \frac{\partial^2\phi}{\partial x^2}\Big|_{0-} = \frac{\eta}{\kappa} \frac{\partial\phi}{\partial x}\Big|_0. \quad (\text{D11})$$

In principle Eq. (D10) can be solved for the partially-wet state. In practice we instead solve the time-dependent problem for  $\phi$  (see Appendix D 4). The system converges to a partially-wet steady state consistent with (D10). Representative examples of full- and partial-wetting solutions are shown in Figure 10 (a,b).

Physically, we note that the pumping term in (D9) acts to increase the magnitude of the density gradient at the origin, and one might imagine that this could create a jump in  $\phi$  (or  $\partial_x\phi$ ). However the term proportional to  $\kappa$  in (D9) strongly suppresses small-wavelength features in  $\phi$ , leading to continuous  $\phi, \partial_x\phi$ , with a jump as in (D11). This is also illustrated in Fig. 10(a).

## 3. Linear stability of the fully-wet state

As noted above, the fully-wet state always exists as a steady-state solution of (D9). However, this state may not be linearly stable. The critical wetting transition corresponds to the onset of linear instability of this state, as in equilibrium [42].

As described in Sec. IV B 2, we find this instability by considering a small perturbation of a homogeneous liquid state. We substitute (46) into (43); the cosine modes in (46) play no role, and we obtain at leading order  $\dot{A}_n = \Gamma_{nm}A_m$  as in (48), with

$$\Gamma_{mn} = -\left(\frac{\alpha}{2}q_n^2 + \kappa q_n^4\right)\delta_{mn} + \frac{2\eta}{L}q_nq_m \quad (\text{D12})$$

(recall  $q_n = 2\pi n/L$ ).

The (infinite) matrix  $\Gamma$  has the form  $\Gamma = D + \beta\mathbf{q}\mathbf{q}^T$ , where  $D = \text{diag}(\{-\frac{\alpha}{2}q_n^2 - \kappa q_n^4\})$  and  $\beta = \frac{2\eta}{L}$ . All the eigenvalues of  $D$  are negative (as  $\alpha, \kappa \geq 0$ ). The Sherman-Morrison formula states, for a rank-1 update of a diagonal matrix:

$$\det(D + \beta\mathbf{q}\mathbf{q}^T - \lambda I) = \det(D - \lambda I)(1 + \beta\mathbf{q}^T(D - \lambda I)^{-1}\mathbf{q}). \quad (\text{D13})$$

The eigenvalues of  $\Gamma$  can therefore be obtained by finding the roots of its characteristic polynomial,  $\det(\Gamma - \lambda I)$ . Using that  $D$  is diagonal we obtain:

$$\begin{aligned} 0 &= \det(D - \lambda I) \left( 1 + \beta \sum_m \frac{q_m q_m}{d_m - \lambda} \right) \\ &= \prod_n (d_n - \lambda) \left( 1 - \beta \sum_m \frac{q_m^2}{\frac{\alpha}{2}q_m^2 + \kappa q_m^4 + \lambda} \right), \end{aligned} \quad (\text{D14})$$

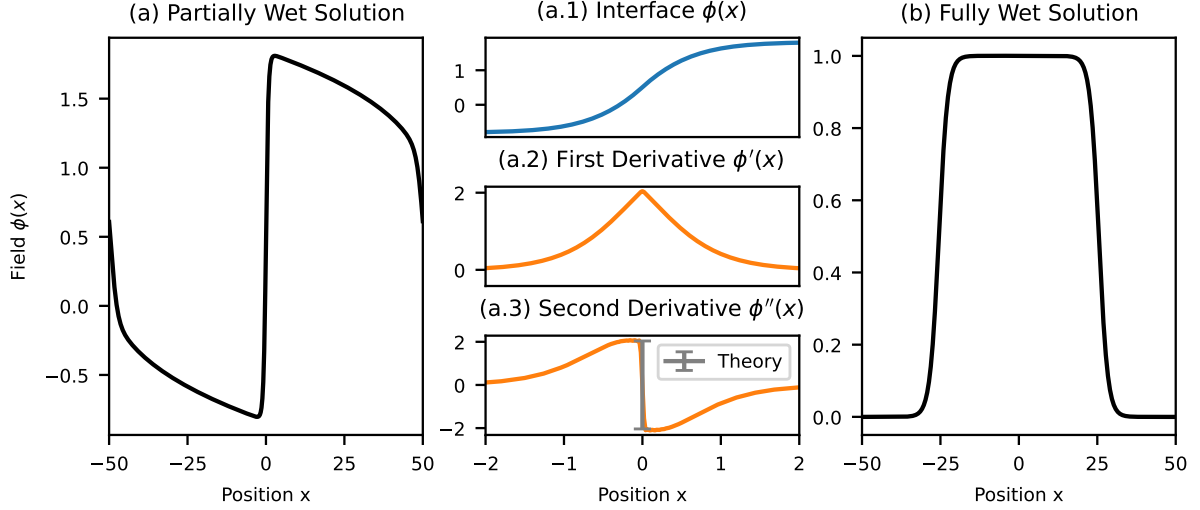


FIG. 10. Representative examples of steady-state full- and partial- wetting solutions in the minimal model. Simulations are run on a grid of size  $N_x = 5001$ , and for model parameters  $\alpha = \kappa = 1$ ,  $L = 100$ ,  $\eta = 2 > \eta^*(\alpha, \kappa)$ , up to  $t_f = 2000$ . (a) Partially-wet solution across the periodic domain, with a pump at  $x = 0$ . (a.1-3) The zoomed-in central interface;  $\phi(x)$ ,  $\phi'(x)$ ,  $\phi''(x)$  are shown for  $x \in [-2, 2]$ . The jump condition (D11) is illustrated in (a.3); the field and its first derivative are continuous, while the second derivative has the expected jump. We can see that the spatial resolution is sufficient to resolve this sharp central interface well. (b) Fully-wet solution, with the same parameters except now  $\eta = 1 < \eta^*$ .

where  $d_m = -\frac{\alpha}{2}q_m^2 - \kappa q_m^4$  are the eigenvalues of  $D$ .

The matrix  $\bar{\Gamma}$  is real-symmetric so its eigenvalues are real. Hence the boundary of linear stability occurs when this matrix has a single zero eigenvalue, with all others being negative. Setting  $\lambda = 0$  and noting that  $d_n < 0$  for all  $n$  we find

$$0 = 1 - \beta \sum_m \frac{1}{(\alpha/2) + \kappa q_m^2}. \quad (\text{D15})$$

Using the identity  $\sum_{n=1}^{\infty} \frac{1}{n^2 + a^2} = \frac{a\pi \coth(a\pi) - 1}{2a^2}$ , with  $a = \frac{L}{2\pi} \sqrt{\frac{\alpha}{2\kappa}}$ , we find the stability boundary to be

$$\frac{2\pi^2\kappa}{\eta L} = \frac{a\pi \coth(a\pi) - 1}{2a^2}, \quad (\text{D16})$$

which we rearrange to obtain an explicit expression for the critical pumping strength  $\eta^*$  at which the system becomes unstable [see Eq. (49)]:

$$\eta^* = \frac{\sqrt{2\alpha\kappa}}{\coth(L\sqrt{\frac{\alpha}{8\kappa}}) - \frac{1}{L}\sqrt{\frac{8\kappa}{\alpha}}}. \quad (\text{D17})$$

For large  $L$ , this tends to  $\sqrt{2\alpha\kappa}$ .

At the onset of instability, the eigenvector  $\mathbf{v}$  whose eigenvalue is 0 (i.e. the most unstable eigenvector) obeys  $D\mathbf{v} = -\beta\mathbf{q}\mathbf{q}^T\mathbf{v}$ . The components of this leading unstable eigenvector can therefore be written explicitly:

$$v_n \propto \frac{1}{q_n \left( \frac{\alpha}{2} + \kappa q_n^2 \right)}. \quad (\text{D18})$$

The eigenfunction which gives rise to instability of the fully-wet state is therefore dominated by large-wavelength modes- this may be expected, as sharp variations in the density profile are suppressed by both the stiffness and chemical potential terms. The consequences of this are discussed in the Section IV B 2.

#### 4. Time-stepping routine for minimal model

For numerical stability and efficiency, we use a spectral scheme to simulate the dynamics of the minimal model. We start with the dynamics in the form:

$$\partial_t \phi(x, t) = -\partial_x^2 \mu + \partial_x(\eta \partial_x \phi \delta(x)) - \kappa \partial_x^4 \phi, \quad (\text{D19})$$

where  $\mu = \frac{\partial f_\phi}{\partial \phi} = \alpha\phi(\phi-1)(\phi-1/2)$ . Applying the standard Fourier transform to both sides  $\phi(x, t) \rightarrow \hat{\phi}(k, t)$ , the dynamics in Fourier space are:

$$\partial_t \hat{\phi}(k, t) = -k^2 \hat{\mu}(k, t) - ik\eta \widehat{J_{\text{pump}}}(k, t) - \kappa k^4 \hat{\phi}(k, t), \quad (\text{D20})$$

where  $\hat{\mu}(k, t)$ ,  $\widehat{J_{\text{pump}}}(k, t)$  are obtained by Fourier transforming  $\mu$ ,  $J_{\text{pump}}$ . We discretise time as  $t_n = n\Delta t$  with intervals  $\Delta t$ . We then follow a standard semi-implicit first-order time-stepping strategy, in which diffusive terms are treated implicitly and other terms explicitly, as described in [75]:

$$\hat{\phi}(k, t_{n+1}) = \frac{\phi(k, t_n) - \Delta t [ik\eta \widehat{J_{\text{pump}}}(k, t_i) + k^2 \hat{\mu}(k, t_n)]}{1 + \kappa k^4 \Delta t}. \quad (\text{D21})$$

In this case, the chemical potential and pumping terms are treated explicitly and evaluated in real space, while the (stiff) diffusive relaxation is treated implicitly in Fourier-space, to give a stable pseudo-spectral update scheme. To implement this, we use a spatial grid  $\{x_j\}$  with  $x_{j+1} - x_j = \Delta x = L/N_x$ , and corresponding discrete Fourier-space frequencies  $k_j = \frac{2\pi j}{L}$ . For the linear stability calculation, we take  $N_x = 2 \times 10^4$ . A time step of  $\Delta t = 10^{-2}$  was found to be sufficient for stable behaviour.

Each timestep proceeds as follows:

1. Starting with the real space field  $\phi_j(t_n) = \phi(x_j, t_n)$ , compute the pumping current as

$$J_{\text{pump}}(L/2, t_n) = \eta \frac{\phi_{(N_x/2)+1}(t_n) - \phi_{(N_x/2)-1}(t_n)}{2\Delta x}, \quad (\text{D22})$$

with  $J_{\text{pump}}(x_j, t) = 0$  at all other spatial points. Similarly compute the chemical potential  $\mu_j(t_n) = \mu(\phi_j, t_n)$ .

2. Compute the discrete Fourier transforms  $\widehat{J_{\text{pump}}}(k_j) =$  and  $\hat{\mu}(k_j)$ .

3. Compute  $\hat{\phi}(k_j, t_{n+1})$  using the semi-implicit dynamics (D21). To suppress numerical artifacts and instability arising from aliasing errors (particularly those introduced by the non-linear chemical potential term) we apply the standard “2/3-rule” [75, 76] de-aliasing procedure in Fourier space, setting all Fourier components with wavenumber  $|k_j| > \frac{2}{3}k_{\text{max}}$  to zero, where  $k_{\text{max}} = \pi/\Delta x$  is the Nyquist frequency associated with the spatial grid.
4. Compute the real-space field  $\phi_j(t_{n+1})$  by inverse Fourier transform of  $\hat{\phi}(k_j, t_{n+1})$ .

It is often convenient to take a centred liquid droplet as an initial condition, approximating the domain walls by tanh profiles. A small noise is added to this initial condition, perturbing each site by Gaussian spatially-white noise with mean zero and variance  $\epsilon = 10^{-4}$ . This initial condition gives rise to the fully-wet state if it is stable, and otherwise reaches the partially-wet state in the long-time limit. To test for stability of the fully wet state, we measure the behaviour of asymmetry over time, as in the full dynamics.

- 
- [1] M. C. Marchetti, J. F. Joanny, S. Ramaswamy, T. B. Liverpool, J. Prost, M. Rao, and R. A. Simha, Hydrodynamics of soft active matter, *Reviews of Modern Physics* **85**, 1143 (2013).
  - [2] S. Ramaswamy, The mechanics and statistics of active matter, *Annual Review of Condensed Matter Physics* **1**, 323 (2010).
  - [3] J. Elgeti, R. G. Winkler, and G. Gompper, Physics of microswimmers—single particle motion and collective behavior: a review, *Reports on Progress in Physics* **78**, 056601 (2015).
  - [4] J. Tailleur and M. E. Cates, Statistical mechanics of interacting run-and-tumble bacteria, *Physical Review Letters* **100**, 218103 (2008).
  - [5] M. E. Cates, Diffusive transport without detailed balance in motile bacteria: does microbiology need statistical physics?, *Reports on Progress in Physics* **75**, 042601 (2012).
  - [6] R. Alert and X. Trepas, Physical models of collective cell migration, *Annual Review of Condensed Matter Physics* **11**, 77 (2020).
  - [7] T. Vicsek, A. Czirók, E. Ben-Jacob, I. Cohen, and O. Shochet, Novel type of phase transition in a system of self-driven particles, *Physical Review Letters* **75**, 1226 (1995).
  - [8] J. Toner and Y. Tu, Flocks, herds, and schools: A quantitative theory of flocking, *Physical Review E* **58**, 4828 (1998).
  - [9] A. Doostmohammadi, J. Ignés-Mullol, J. M. Yeomans, and F. Sagués, Active nematics, *Nature Communications* **9**, 3246 (2018).
  - [10] A. Walther and A. H. E. Müller, Janus particles: Synthesis, self-assembly, physical properties, and applications, *Chemical Reviews* **113**, 5194 (2013).
  - [11] B. Saintyves, M. Spenko, and H. M. Jaeger, A self-organizing robotic aggregate using solid and liquid-like collective states, *Science Robotics* **9** (2024).
  - [12] M. E. Cates and J. Tailleur, Motility-induced phase separation, *Annual Review of Condensed Matter Physics* **6**, 219 (2015).
  - [13] M. E. Cates and C. Nardini, Active phase separation: new phenomenology from non-equilibrium physics, *Reports on Progress in Physics* **88**, 056601 (2025).
  - [14] M. E. Cates and J. Tailleur, When are active brownian particles and run-and-tumble particles equivalent? consequences for motility-induced phase separation, *EPL (Europhysics Letters)* **101**, 20010 (2013).
  - [15] Y. Fily and M. C. Marchetti, Athermal phase separation of self-propelled particles with no alignment, *Phys. Rev. Lett.* **108**, 235702 (2012).
  - [16] G. S. Redner, M. F. Hagan, and A. Baskaran, Structure and dynamics of a phase-separating active colloidal fluid, *Phys. Rev. Lett.* **110**, 055701 (2013).
  - [17] P. Digregorio, D. Levis, A. Suma, L. F. Cugliandolo, G. Gonnella, and I. Pagonabarraga, Full phase diagram of active brownian disks: From melting to motility-induced phase separation, *Physical Review Letters* **121**, 098003 (2018).
  - [18] R. Wittkowski, A. Tiribocchi, J. Stenhammar, R. J. Allen, D. Marenduzzo, and M. E. Cates, Scalar  $\phi^4$  field theory for active-particle phase separation, *Nat. Comms.* **5**, 4351 (2014).
  - [19] E. Tjhung, C. Nardini, and M. E. Cates, Cluster phases and bubbly phase separation in active fluids: Reversal of the ostwald process, *Physical Review X* **8**, 031080 (2018).
  - [20] Y. Ben Dor, S. Ro, Y. Kafri, M. Kardar, and J. Tailleur, Disordered boundaries destroy bulk phase separation in scalar active matter, *Physical Review E* **105**, 044603 (2022).

- (2022).
- [21] P. Galajda, J. Keymer, P. Chaikin, and R. Austin, A wall of funnels concentrates swimming bacteria, *Journal of Bacteriology* **189**, 8704 (2007).
  - [22] C. O. Reichhardt and C. Reichhardt, Ratchet effects in active matter systems, *Annual Review of Condensed Matter Physics* **8**, 51 (2017).
  - [23] C. Bechinger, R. Di Leonardo, H. Löwen, C. Reichhardt, G. Volpe, and G. Volpe, Active particles in complex and crowded environments, *Reviews of Modern Physics* **88**, 045006 (2016).
  - [24] S. Das, G. Gompper, and R. G. Winkler, Confined active brownian particles: theoretical description of propulsion-induced accumulation, *New Journal of Physics* **20**, 015001 (2018).
  - [25] M. Mangeat, S. Chakraborty, A. Wysocki, and H. Rieger, Stationary particle currents in sedimenting active matter wetting a wall, *Physical Review E* **109**, 014616 (2024).
  - [26] J. Stenhammar, R. Wittkowski, D. Marenduzzo, and M. E. Cates, Light-induced self-assembly of active rectification devices, *Science Advances* **2** (2016).
  - [27] J. Metzger, S. Ro, and J. Tailleur, Revisiting the ratchet principle: When hidden symmetries prevent steady currents (2024), arXiv:2412.07851 [cond-mat.stat-mech].
  - [28] J. Metzger, S. Ro, and J. Tailleur, Exceptions to the ratchet principle in active and passive stochastic dynamics (2025), arXiv:2503.11902 [cond-mat.stat-mech].
  - [29] O. Granek, Y. Kafri, M. Kardar, S. Ro, J. Tailleur, and A. Solon, Colloquium : Inclusions, boundaries, and disorder in scalar active matter, *Reviews of Modern Physics* **96**, 031003 (2024).
  - [30] F. Turci and N. B. Wilding, Wetting transition of active brownian particles on a thin membrane, *Physical Review Letters* **127**, 238002 (2021).
  - [31] F. Turci, R. L. Jack, and N. B. Wilding, Partial and complete wetting of droplets of active brownian particles, *Soft Matter* **20**, 2060 (2024).
  - [32] P. D. Neta, M. Tasinkevych, M. M. Telo da Gama, and C. S. Dias, Wetting of a solid surface by active matter, *Soft Matter* **17**, 2468 (2021).
  - [33] J. Elgeti and G. Gompper, Wall accumulation of self-propelled spheres, *EPL (Europhysics Letters)* **101**, 48003 (2013).
  - [34] M. Rojas-Vega, P. de Castro, and R. Soto, Wetting dynamics by mixtures of fast and slow self-propelled particles, *Physical Review E* **107**, 014608 (2023).
  - [35] M. Rojas-Vega, P. de Castro, and R. Soto, Mixtures of self-propelled particles interacting with asymmetric obstacles, *The European Physical Journal E* **46**, 95 (2023).
  - [36] P. Perez-Bastías and R. Soto, Two-field theory for phase coexistence of active brownian particles (2025), arXiv:2504.13327 [cond-mat.soft].
  - [37] N. Sepúlveda and R. Soto, Wetting transitions displayed by persistent active particles, *Physical Review Letters* **119**, 078001 (2017).
  - [38] N. Sepúlveda and R. Soto, Universality of active wetting transitions, *Physical Review E* **98**, 052141 (2018).
  - [39] S. Das and R. Chelakkot, Morphological transitions of active brownian particle aggregates on porous walls, *Soft Matter* **16**, 7250 (2020).
  - [40] L. Caprini, D. Breoni, A. Ldov, C. Scholz, and H. Löwen, Dynamical clustering and wetting phenomena in inertial active matter, *Communications Physics* **7**, 343 (2024).
  - [41] P. G. de Gennes, Wetting: statics and dynamics, *Rev. of Mod. Phys.* **57**, 827 (1985).
  - [42] J. W. Cahn, Critical point wetting, *J. Chem. Phys.* **66**, 3667 (1977).
  - [43] D. Bonn, J. Eggers, J. Indekeu, J. Meunier, and E. Rolley, Wetting and spreading, *Reviews of Modern Physics* **81**, 739 (2009).
  - [44] S. Dietrich, Wetting phenomena, *Phase Transitions and Critical Phenomena* **12**, 1 (1988).
  - [45] A. M. Tayar, F. Caballero, T. Anderberg, O. A. Saleh, M. Cristina Marchetti, and Z. Dogic, Controlling liquid-liquid phase behaviour with an active fluid, *Nature Materials* **22**, 1401 (2023).
  - [46] S. Douezan, K. Guevorkian, R. Naouar, S. Dufour, D. Cuvelier, and F. Brochard-Wyart, Spreading dynamics and wetting transition of cellular aggregates, *Proceedings of the National Academy of Sciences* **108**, 7315 (2011).
  - [47] R. Hartmann, P. K. Singh, P. Pearce, R. Mok, B. Song, F. Díaz-Pascual, J. Dunkel, and K. Drescher, Emergence of three-dimensional order and structure in growing biofilms, *Nature Physics* **15**, 251 (2018).
  - [48] E. Lauga, W. R. DiLuzio, G. M. Whitesides, and H. A. Stone, Swimming in circles: Motion of bacteria near solid boundaries, *Biophysical Journal* **90**, 400 (2006).
  - [49] Y. I. Yaman, E. Demir, R. Vetter, and A. Kocabas, Emergence of active nematics in chaining bacterial biofilms, *Nature Communications* **10**, 2285 (2019).
  - [50] L. Chai, V. Zaburdaev, and R. Kolter, How bacteria actively use passive physics to make biofilms, *Proceedings of the National Academy of Sciences* **121**, 40 (2024).
  - [51] R. M. Harshey, Bacterial motility on a surface: Many ways to a common goal, *Annual Review of Microbiology* **57**, 249 (2003).
  - [52] C. Pérez-González, R. Alert, C. Blanch-Mercader, M. Gómez-González, T. Kolodziej, E. Bazellieres, J. Casademunt, and X. Trepat, Active wetting of epithelial tissues, *Nature Physics* **15**, 79 (2018).
  - [53] A. Brugués, E. Anon, V. Conte, J. H. Veldhuis, M. Gupta, J. Colombelli, J. J. Muñoz, G. W. Brodland, B. Ladoux, and X. Trepat, Forces driving epithelial wound healing, *Nature Physics* **10**, 683 (2014).
  - [54] J. F. Joanny, K. Kruse, J. Prost, and S. Ramaswamy, The actin cortex as an active wetting layer, *The European Physical Journal E* **36**, 52 (2013).
  - [55] Y. Zhao, R. Zakine, A. Daerr, Y. Kafri, J. Tailleur, and F. van Wijland, Active young-dupré equation: How self-organized currents stabilize partial wetting (2024), arXiv:2405.20651 [cond-mat.soft].
  - [56] J. Bialké, J. T. Siebert, H. Löwen, and T. Speck, Negative interfacial tension in phase-separated active brownian particles, *Physical Review Letters* **115**, 098301 (2015).
  - [57] R. Adkins, I. Kolvin, Z. You, S. Witthaus, M. C. Marchetti, and Z. Dogic, Dynamics of active liquid interfaces, *Science* **377**, 768 (2022).
  - [58] A. P. Solon, Y. Fily, A. Baskaran, M. E. Cates, Y. Kafri, M. Kardar, and J. Tailleur, Pressure is not a state function for generic active fluids, *Nature Physics* **11**, 673–678 (2015).
  - [59] M. Kourbane-Houssene, C. Erignoux, T. Bodineau, and J. Tailleur, Exact hydrodynamic description of active lattice gases, *Physical Review Letters* **120**, 268003 (2018).
  - [60] J. Mason, C. Erignoux, R. L. Jack, and M. Bruna, Exact hydrodynamics and onset of phase separation for an active exclusion process, *Proceedings of the Royal Society*

- A: Mathematical, Physical and Engineering Sciences **479** (2023).
- [61] C. Erignoux, On the hydrodynamics of active matter models on a lattice, *Markov Processes And Related Fields* **30**, 57 (2024).
  - [62] D. Martin, D. Seara, Y. Avni, M. Fruchart, and V. Vitelli, The transition to collective motion in nonreciprocal active matter: coarse graining agent-based models into fluctuating hydrodynamics (2024), arXiv:2307.08251 [cond-mat.stat-mech].
  - [63] J. Mason, R. L. Jack, and M. Bruna, Dynamical patterns and nonreciprocal effective interactions in an active-passive mixture through exact hydrodynamic analysis (2025), arXiv:2408.03932 [cond-mat.stat-mech].
  - [64] R. Evans, M. C. Stewart, and N. B. Wilding, A unified description of hydrophilic and superhydrophobic surfaces in terms of the wetting and drying transitions of liquids, *Proceedings of the National Academy of Sciences* **116**, 23901 (2019).
  - [65] P.-G. de Gennes, F. Brochard-Wyart, and D. Quéré, *Capillarity and Wetting Phenomena: Drops, Bubbles, Pearls, Waves* (Springer, New York, 2003).
  - [66] X.-T. Wu, D. Abraham, and J. Indekeu, Apparent first-order wetting and anomalous scaling in the two-dimensional ising model, *Physical Review Letters* **116**, 046101 (2016).
  - [67] K. Binder, D. Landau, and M. Müller, Monte carlo studies of wetting, interface localization and capillary condensation, *Journal of Statistical Physics* **110**, 1411 (2003).
  - [68] A. Drzewiński, A. Maciolek, A. Barasiński, and S. Dietrich, Critical wetting transitions in two-dimensional systems subject to long-ranged boundary fields, *Physical Review E* **79**, 041144 (2009).
  - [69] J. Mason, R. L. Jack, and M. Bruna, Macroscopic behaviour in a two-species exclusion process via the method of matched asymptotics, *Journal of Statistical Physics* **190**, 47 (2023).
  - [70] J. Eggers, Sand as maxwell's demon, *Physical Review Letters* **83** (1999).
  - [71] J. Sherman and W. J. Morrison, Adjustment of an inverse matrix corresponding to a change in one element of a given matrix, *The Annals of Mathematical Statistics* **21**, 124 (1950).
  - [72] H. R. Vutukuri, M. Lisicki, E. Lauga, and J. Vermant, Light-switchable propulsion of active particles with reversible interactions, *Nature Communications* **11**, 2628 (2020).
  - [73] M. Rey, G. Volpe, and G. Volpe, Light, matter, action: Shining light on active matter, *ACS Photonics* **10**, 1188 (2023).
  - [74] <https://github.com/SoftMatterGroupCambridge/ActiveWettingHydrodynamics>.
  - [75] J. P. Boyd, *Chebyshev and Fourier spectral methods* (Dover Publications, 2013) pp. 211–213, 229–230.
  - [76] S. A. Orszag, On the elimination of aliasing in finite-difference schemes by filtering high-wavenumber components, *Journal of the Atmospheric Sciences* **28**, 1074 (1971).